Article

Evidence of Dextral Strike-Slip Movement of the Alakol Lake Fault in the Western Junggar Based on Remote Sensing

Wenxing Yi [1], An Li [1,*], Liangxin Xu [2], Zongkai Hu [1] and Xiaolong Li [1]

1   State Key Laboratory of Earthquake Dynamics, Institute of Geology, China Earthquake Administration, Beijing 100029, China; yiwenxing@ies.ac.cn (W.Y.)
2   Academy of Seismic Engineering Surveys, Earthquake Administration of Shaanxi Province, Xi'an 710068, China
*   Correspondence: lian@ies.ac.cn

Abstract: The NW-SE-trending dextral strike-slip faults on the north side of the Tian Shan, e.g., the Karatau fault, Talas–Fergana fault, Dzhalair–Naiman fault, Aktas fault, Dzhungarian fault, and Chingiz fault, play an important role in accommodating crustal shortening. The classic viewpoint is that these strike-slip faults are an adjustment product caused by the difference in the crustal shortening from west to east. Another viewpoint attributes the dextral strike-slip fault to large-scale sinistral shearing. The Alakol Lake fault is a typical dextral strike-slip fault in the north Tian Shan that has not been reported. It is situated along the northern margin of the Dzhungarian gate, stretching for roughly 150 km from Lake Ebinur to Lake Alakol. Our team utilized aerial photographs, satellite stereoimagery, and field observations to map the spatial distribution of the Alakol Lake fault. Our findings provided evidence supporting the assertion that the fault is a dextral strike-slip fault. In reference to its spatial distribution, the Lake Alakol is situated in a pull-apart basin that lies between two major dextral strike-slip fault faults: the Chingiz and Dzhungarian faults. The Alakol Lake fault serves as a connecting structure for these two faults, resulting in the formation of a mega NW-SE dextral strike-slip fault zone. According to our analysis of the dating samples taken from the alluvial fan, as well as our measurement of the displacement of the riser and gully, it appears that the Alakol Lake fault has a dextral strike-slip rate of 0.8–1.2 mm/a (closer to 1.2 mm/a). The strike-slip rate of the Alakol Lake fault is comparatively higher than that of the Chingiz fault in the northern region (~0.7 mm/a) but slower than that of the Dzhungarian fault in the southern region (3.2–5 mm/a). The Chingiz–Alakol–Dzhungarian fault zone shows a gradual decrease in deformation towards the interior of the Kazakhstan platform.

Keywords: Alakol Lake fault; dextral strike-slip; slip rate; UAV photogrammetry; satellite stereoimagery

1. Introduction

Central Asia has experienced extensive Cenozoic deformation and developed a large amount of active orogenic belts due to the impact of the India–Eurasia collision [1,2]. One of the most representative and significant orogenic belts is the Tian Shan, which underwent reactivation in the Cenozoic [3–6]. The Tian Shan is an active intracontinental orogenic belt that extends east–west for 2500 km and south–north for 250–350 km. In the Quaternary, the Tian Shan underwent strong tectonic deformation, such as compression and uplift, and rapid north–south crustal shortening [3,7–11]. Faults in the Tian Shan, including E-W-trending thrust faults [3,12–15], ENE-WSW-trending sinistral strike-slip faults [2,16,17], and NW-SE-trending dextral strike-slip faults [18–20], accommodated the crustal shortening. The GPS data indicate that the total shortening rate is approximately 20 mm/a across the western Tian Shan to the Kazakh platform, which is nearly half of the total convergence rate between India and Eurasia [21–24]. The NW-SE dextral strike-slip faults on the north side

of the Tian Shan, e.g., the Karatau fault, Talas–Ferganas fault, Dzhalair–Naiman fault, Aktas fault, Dzhungarian fault (also named the Bolokenu–Aqikekuduk fault), and the Chingiz fault, play a crucial role in accommodating crustal shortening [2,19,25]. Some geodynamic mechanisms of the Tian Shan region suggest that the strike-slip faults are an adjustment product caused by the difference in east–west crustal shortening [2,3,26]. At the same time, based on GPS velocities, some researchers attribute the dextral strike-slip fault to large-scale sinistral shearing [27,28]. It is worth noting that other researchers have recognized the strike-slip characteristics of the fault related to block movement and rotation [17,21]. Therefore, it is significant to obtain and understand the activity characteristics of strike-slip faults for tectonic deformation in the Tian Shan.

The Dzhungarian fault (DZF) is a large NW-SE-trending dextral strike-slip fault, which extends for more than 700 km and constitutes the boundary fault between the north Tian Shan and the middle Tian Shan (Figure 1a) [19,20,25,29]. Previous studies revealed that the Dzhungarian fault had a slip rate of 2.2–3.2 mm/a in its middle segment [19,20] and a rate of ~1.7 mm/a at the end of the northwest segment in the late Quaternary [30]. The Chingiz fault (CF) is an NW-SE-trending dextral strike-slip fault that runs for over 600 km in the east–central Kazakhstan platform [31,32]. Distinct linear traces along the Chingiz fault can be observed from Landsat satellite images [32]. In the Cenozoic, the Chingiz fault has typical dextral strike-slip characteristics with a small thrust component [31]. The GPS data indicate ~0.7 mm/a as the dextral strike-slip rate in the Chingiz fault [33]. The Dzhungarian fault and the Chingiz fault are more than 100 km apart and arranged in right steps en echelon, with Lake Alakol in the stepover. A nearly 150 km long fault along the northeast of Lake Alakol to Dzhungarian gate is called the Alakol Lake fault (ALF).
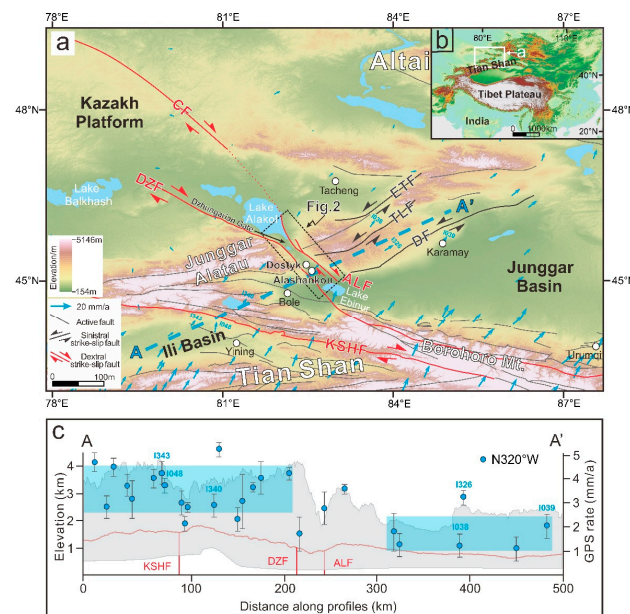

Figure 1. (**a**) The digital elevation model shows the distribution of the main Quaternary faults in the northern Tian Shan region (modified after Xu et al., 2016) [34]. Blue arrows show the GPS measurements from Wang and Shen (2020) [23]. The blue dashed lines (A–A') show the locations of the GPS profiles. The white circles show the major cities. The black dashed boxes show the locations of Figure 2. DZF—Dzhungarian fault; ALF—Alakol Lake fault; CF—Chingiz fault; KSHF—Kashihe fault; ETF—East Tacheng fault; TLF—TuoLi fault; and DF—Daerbute fault. (**b**) The global digital elevation model shows the tectonic location of the research area (**a**). (**c**) Swath GPS profile A–A' shows the velocity components parallel to (blue dots) the profile striking N320°W [20]. The brown line and gray shadow show the mean value and range of elevation with 50 km width along the profile A–A'. The blue-shaded rectangles are the visually fitted range of the GPS velocities. The blue letters and numbers represent the GPS observation stations' abbreviations.
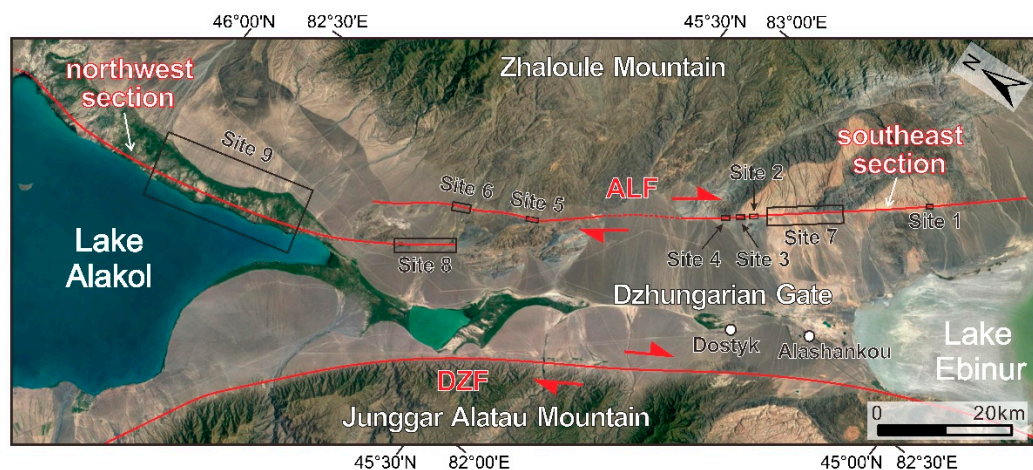
Figure 2. The extension of the Alakol Lake fault is shown on Google Earth. The red lines show the location of the fault trace. The red triangular arrows indicate dextral strike-slip movement. The black boxes are the study sites. The white circles show the major cities.

The GPS velocities with respect to Eurasia decrease from ~4 mm/a in the Ili Basin to less than 2 mm/a in the northwest margin of the Junggar Basin, indicating that the DZF and ALF accommodate around 2 mm/a of crustal shortening at N320°W (Figure 1c) [20]; however, it is still unclear what the geometric characteristics of the ALF are and how it absorbs crustal shortening. Furthermore, from the spatial distribution of the ALF, it connects the CF and the DZF (Figure 1a). All in all, it is significant to study the activity characteristics of these faults in the Quaternary to understand the tectonic deformation in the Tian Shan. Exploring the geometric structure and kinematic characteristics of the ALF is essential for understanding its structural relationship and block deformation with the two large strike-slip faults (DZF and CF). Otherwise, the Dzhungarian gate is a geographically and historically significant mountain pass between China and Central Asia. Furthermore, the Alakol Lake fault is located near the important trade ports of Alashankou in China and Dostyk in Kazakhstan. Therefore, investigating the kinematic properties of the fault can provide basic data for assessing seismic hazards in these cities and regions in the future.

In this study, we identified the dextral strike-slip characteristics of the ALF using high-precision aerial photographs, satellite stereoimagery, and field observations. We then described the detailed fault traces and tectonic features, such as alluvial fan surfaces, gullies, offset stream channels, and fault scarps, based on the obtained data. Finally, we discussed the role of the ALF in the tectonic pattern formed in the north of the Tian Shan.

2. Geological Setting

The western Junggar is a significant part of the Central Asian orogenic belts, which lies between the Kazakh platform to the west, the Junggar Basin to the east, the Borohoro Mountain range to the south, and the Altai Shan to the north (Figure 1a). The western Junggar has undergone a multiple-stage orogenic evolution since the Early Paleozoic, including the multiple-phase subduction of the Paleo-Asian oceanic plate, crustal accretion, and continental growth [35–37]. This region primarily consists of a series of accretionary complex belts and Paleozoic magmatic arcs [38,39]. The main exposed strata in the western Junggar are volcanic sedimentary strata from the Ordovician to the Carboniferous, and the most widely distributed are Carboniferous thick pyroclastic sedimentary formations. The magmatic activity in the western Junggar area was particularly intense in the late Paleozoic, and granites with positive εNd(t) and low initial ^{87}Sr/^{86}Sr characteristics were widely distributed in the region [40–43]. In the western Junggar, large sinistral and dextral strike-slip faults are mainly developed. The sinistral strike-slip faults include the ENE-WSW-trending Daerbute fault (DF), TuoLi fault (TLF), and East Tacheng fault (ETF) (Figure 1a).

The dextral strike-slip faults include the NW-SE-trending Chingiz fault (CF), Dzhungarian fault (DZF), and Kashihe fault (KSHF) (Figure 1a).

The Junggar Alatau is located in the north of the western Tian Shan, and the overall trend is nearly east–west (Figure 1a). The Alatau Mountain is at the border between China and Kazakhstan, an important part of the Central Asian orogenic belts. The Junggar Alatau developed in the Upper Paleozoic and the Cenozoic and was absent in the Mesozoic [44,45]. The bedrock of the Junggar Alatau is well exposed, and the strata are mainly late Paleozoic clastic rocks and carbonate rocks. There were also frequent magmatic activities in the late Paleozoic, a large distribution area of igneous rocks, and diverse rock types in the Junggar Alatau [46].

The ALF lies in the western Junggar, which extends about 150 km from the northeast of Lake Ebinur (45°1′N, 82°59′E) to the eastern end of Lake Alakol (46°8′N, 82°1′E) (Figure 1a). The ALF can be divided into two sections by a compression ridge based on the distribution of the fault trace. The northwest section is located to the east of Lake Alakol, extending for ~70 km. The southeast section is distributed to the west of the Zhaloule Mountain, extending for ~80 km (Figure 2). The strike of the ALF is from 315° to 330°, and the overall strike of the fault is 320°. According to the 1:500,000 geological map compiled by China, previous research dates, and field observations, the bedrocks around the Alakol Lake fault are Paleozoic rocks, mainly including Ordovician marine sedimentary rocks and Carboniferous volcanic rocks [47]. Combined with the field investigation, the geomorphic surface of the area of the ALF is mainly Quaternary alluvial deposit and Gobi material.

3. Methods

3.1. Drone Digital Elevation Models and Other Image Data

In the research on the Alakol Lake fault, we require a set of quantitative parameters in order to elucidate its kinematic characteristics, activity intensity, and activity patterns. These parameters include the horizontal displacement of the alluvial fan surfaces, stream channels, gullies, and ridges; the vertical displacement of the fault scarps; and the age of these geomorphic surfaces [48–50]. High-precision and high-resolution topographic and geomorphic data that can reveal subtle geomorphic features are the basis of the quantitative study of active structures [49,51]. We achieved these conditions using the core concept of structure from motion (SfM), a photo-based technique for three-dimensional (3D) reconstruction to create a high-resolution digital elevation model (DEM) [52–54]. SfM is a technique with which to reconstruct a 3D scene from multiple flat images, and it can recover the relative position and attitude of the camera from a disordered image with a certain overlap degree via image feature extraction and matching [55]. Using the structure from motion (SfM) technique, we employ an unmanned aerial vehicle (UAV) (DJI Phantom 4 RTK) to create orthoimages and high-resolution DEMs with a pixel resolution of less than 0.1 m. In these areas where we use the UAV, the UAV flies at a height of 120–220 m, with 70% forward and side overlaps at each site. Through this process, we obtained hundreds of images with a resolution of 5472 pixels in width and 3648 pixels in height for each site. These images of each site were generated using high-resolution DEM software (Pix4Dmapper 4.4.10) integrated with SfM algorithms. DEMs with a resolution of less than 10 cm can clearly display various topographic indexes, such as hillshades, contour lines, and slopes.

When observing large-scale landforms, using a UAV photogrammetry technique based on SfM may not be sufficient to achieve the desired effect; therefore, utilizing Pleiades satellite images to generate high-resolution DEMs is another effective method. We use two stereo pairs of Pleiades images to construct a 0.5 m resolution DEM, and the detailed methods mainly followed those of Zhou et al. (2015) and Wang et al. (2019) [56,57]. The 0.5 m resolution of the DEM is high enough to identify hundreds of meters of horizontal offsets of alluvial fans and displacements of stream channels.

However, due to certain conditions, it is still difficult to obtain high-resolution DEMs in some regions, especially the ~70 km long fault of the northwest section (in Kazakhstan).

Therefore, using Google Earth to extract images to identify the kinematic evidence in the northwest section is an extremely efficient and convenient method to reveal the fault trace and displaced stream channels.

3.2. Offset Measurements of Landforms

The displacement of a fault can be measured by the distance between two correlation marker units projected onto the fault trace [49,58,59]. Additionally, confidence ratings express the reliability of the original morphology of the offset markers, and an offset range is assigned to every measurement to describe the physically plausible range of an offset measurement [49,60,61].

Alluvial fans are typically formed when flowing water interacts with mountains. The mountain on the north side of the ALF brought many material sources and formed multiple alluvial fans in front of the hill. The size and shape of these fans were identified using the orthoimage and DEM. Then, we checked each horizontal offset feature and traced the channel or the riser of the alluvial fans on both sides of the fault as a straight line. The next step was to measure the distances between the projections of upstream and downstream fitted straight lines onto the fault plane. Due to lateral erosion of the channel near the fault, it is difficult to trace an accurate offset landform [58]. We measured the maximum and minimum offset possibilities and expressed the form with the average value and error type to identify the offset range. As a result, the offset range does not represent a confidence interval.

The width of a gully and ridge is usually less than the width of a stream channel, so we can directly make linear fittings of the gully (bottom of the gully) and ridge (top of the ridge) on both sides of the fault trace. The projections of the fitted line onto the fault are measured as the horizontal offset. Their offset range is measured similarly to that of the stream channel.

Different fault scarps of varying heights were formed along the fault on various geomorphic surfaces due to the vertical displacement of the fault. To obtain the vertical displacement, well-preserved scarps were mapped and identified based on the high-resolution UAV DEM. Then, topographic profiles perpendicular to the fault scarp were extracted. The topographic profiles of the hanging wall and footwall were linearly regressed by two separate straight lines. The vertical distances of the two fitted lines projected onto the fault trace were measured to represent the vertical displacement.

In this paper, a method called "Back-slipping" was used to measure the lateral offsets of the gullies. After the fault trace and two separated geomorphic marker sections were identified, we back-slipped them along the fault trace to reconstruct the original morphology of the geomorphic markers and determine the offset [61–63].

3.3. Chronology Dating

Optically stimulated luminescence (OSL) dating is one of the methods of luminescence dating, which can determine the age of sedimentary strata by measuring the equivalent dose (De, which is the ionizing radiation dose corresponding to the natural OSL signal intensity of quartz and other minerals in the sediment) and the environmental dose rate received by the sample per year (D) [64–66]. The age of sedimentary strata is calculated as follows:

$$Age = De/D$$

The unit of age is ka. The unit of De is Gy. The unit of D is Gy/ka.

In this research, three OSL samples (AL-01, AL-04, and AL-05) were collected from the capping loess in the alluvial fans, and two OSL samples (AL-02 and AL-03) were collected from the trench wall in the alluvial fans. All the samples were carefully collected and sealed in opaque iron tubes. These samples were processed and measured at the National Institute of Natural Hazards, the Ministry of Emergency Management of China. The sample pretreatment followed the experimental procedure of Aitken (1998) and Lu et al. (2007), and then relatively pure quartz particles were obtained [67,68]. The equivalent dose (De) was measured using

the methods of Murray et al. (2000, 2003) [65,69]. The effects of radionuclides and cosmic rays were measured to determine the dose rate received per year (D) [67,70].

4. Results

4.1. Distribution of the Study Site

Seven study sites were selected along the southeast section of the Alakol Lake fault in China, and two interpretation sites were selected near Lake Alakol in Kazakhstan (Figure 2). The high-resolution DEMs from aerial photography and some field observations were displayed at these seven sites to describe the southeast section of the ALF. At sites 7 and 8, we also utilized Pleiades satellite images to generate high-resolution DEMs over a large spatial range. In the northwest section, we observed geomorphological characters and displacements using the DEMs at site 8, while at site 9, we identified the fault trace and horizontal offsets using the Google Earth image and surveyed the vertical displacement in the DEMs.

4.2. Geomorphic Development and Dating

By identifying the height above the channel of the alluvial fan and assessing the subgully erosion on the alluvial fan surface, we divide these alluvial fans into four stages, which are named T1, T2, T3, and T4, from most recent to oldest. T1 is the lowest alluvial fan, which is 1–6 m high above the channel. T2 and T3 are 18–20 m and 24–50 m above the stream bed, respectively. T4 is the highest alluvial fan in the study area, preserved well and more than 50 m above the stream bed. The alluvial fan which is older than T4 has been eroded into pieces.

Five OSL samples were collected in order to date the geomorphic surface ages in this research. The sample AL-01 was collected from the coarse-grain sand layer at a ~0.8 m depth below the surface of the T2 alluvial fan at site 4 (Figure 3a). The OSL age of the sample AL-01 indicates a sedimentary age of 24.57 ± 1.72 ka. The sample AL-02 was collected from the coarse-grain sand layer at a depth of ~1 m below the surface of T2 at site 5, which dated the age of T2 at 22.23 ± 1.06 ka (Figure 3b). The sample AL-03 was also collected from the coarse-grain sand layer at a depth of ~5 m below the T3 surface at the riser, which estimated a minimum dating result of 76.01 ± 5.64 ka for T3 (Figure 3c). Because the burial depth of the sampling location is too deep below the surface, even the minimum dating result may overestimate the formation age of the T3 alluvial fan. Along the fault trace, sample AL-04 was collected from the T1 alluvial fan, ~1.5 km northwest of site 4. The sample AL-04 was collected from the fine-grain sand layer at ~1.0 m below the surface of the T1 alluvial fan, which OSL-dated it with an age of 2.68 ± 0.16 ka (Figure 3d). A fault scarp displaced this T1 alluvial fan, indicating the fault activity in the Holocene (Figure 3e). Sample AL-05 was collected from the T2 alluvial fan, ~1 km southeast of site 2. The sample AL-05 was collected from the coarse-grain sand layer at a ~1.8 m depth below the surface of the T2 alluvial fan, which is ~18 m high above the stream bed (Figure 3f). The dating of the sample AL-05 is 16.34 ± 1.06 ka.

Previous studies on the DZF, which is located on the southeast side of the Dzhungarian gate, have dated the alluvial fan. In cases where alluvial fans share a base level, the age of the geomorphic surfaces along the ALF can be referenced against the age of alluvial fans with a similar height above the channel in the area of the DZF. Campbell et al. (2013) determined the age of the alluvial fan by using optically stimulated luminescence (OSL) to date the fine-grained quartz-rich fluvial sediment. The sample site is only ~18 km west of our study area. The OSL age of the fan is 25.7 ± 5.8 ka, and the alluvial fan is ~12 m high above the modern channel [19]. In our study, T2 at site 5 is ~18 m high above the channel, which is close to the height of the alluvial fan studied by Campbell (~12 m). Furthermore, the age, 22.23 ± 1.06 ka, of the T2 alluvial fan at site 5 is close to the age, 25.7 ± 5.8 ka, of the alluvial fan that was dated by Campbell.
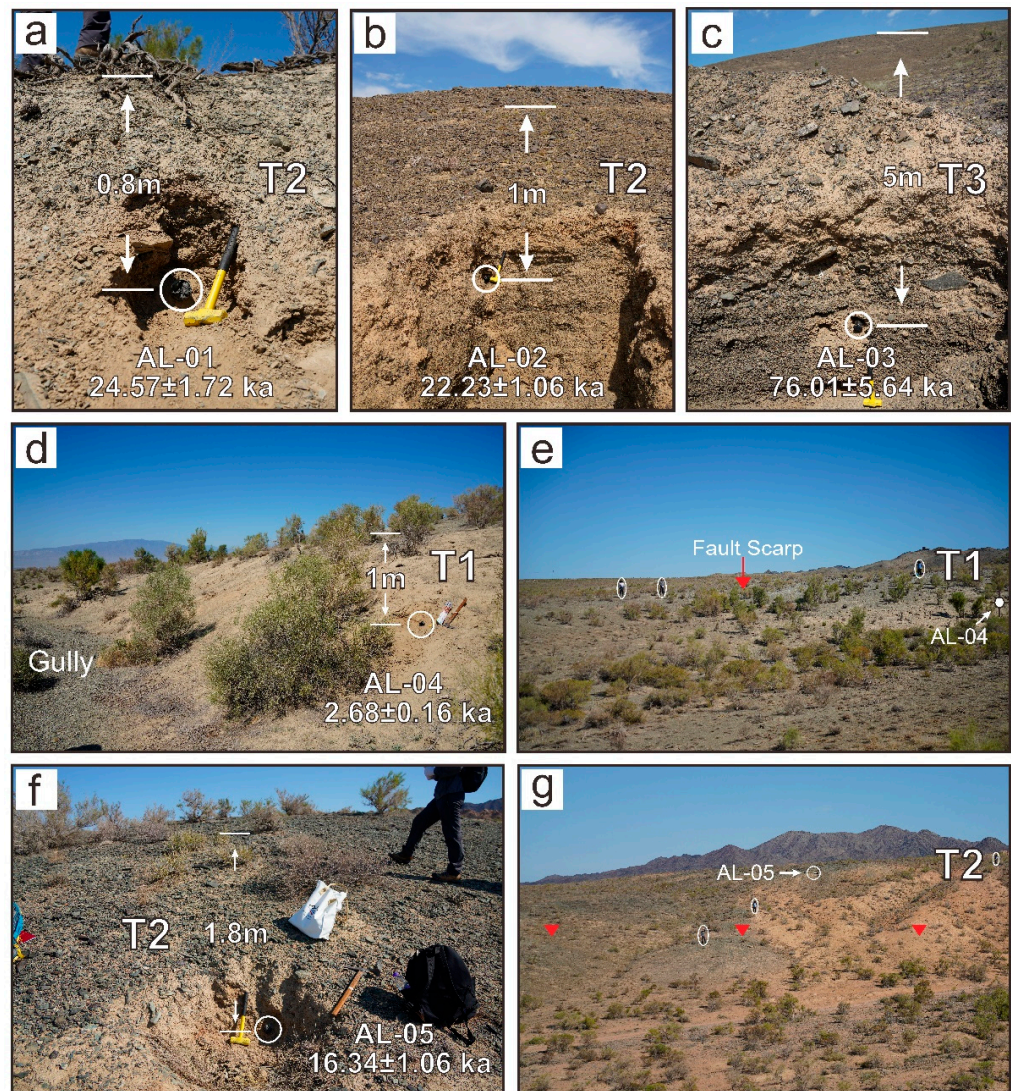
Figure 3. Field collection locations of the OSL samples: (**a**) sample AL-01; (**b**) sample AL-02; (**c**) sample AL-03; and (**d**) sample AL-04. (**e**) The field site shows a dextral alluvial fan and the fault scarp, which is also where the sample AL-04 was collected. (**f**) Sample AL-05. (**g**) The field site indicates the fault trace and fault scarp, which is also where the sample AL-05 was collected. The red triangular arrows indicate the fault trace.

Based on the ages of the sedimentary deposits and the heights of the alluvial fans above the channel, we believe that the alluvial fans, which have similar heights above the channel, have similar formation periods near the Dzhungarian gate. The formation ages of T1–T3 are 2–3 ka, ~20 ka, and less than 76 ka, respectively. Detailed OSL dating results for the five samples are shown in Table 1.

Table 1. OSL dating results.

Sample ID	Sample Coordinate	Depth (m)	U (ppm)	Th (ppm)	K (%)	Water Content (%)	D (Gy/ka)	De_{MAM} (Gy)	Age_{MAM} (ka)	De_{CAM} (Gy)	Age_{CAM} (ka)	De_{AVG} (Gy)	Age_{AVG} (ka)
AL-01	45°21′01″N 82°38′56″E	0.8	2.12 ± 0.01	6.57 ± 0.08	1.69 ± 0.01	5	2.73 ± 0.11	39.7 ± 3.15	14.57 ± 1.3	64.24 ± 3.91	23.57 ± 1.72	66.96 ± 3.81	24.57 ± 1.72
AL-02	45°32′24″N 82°26′29″E	1	1.55 ± 0.04	4.6 ± 0.11	1.59 ± 0.01	5	2.37 ± 0.1	49.53 ± 2.59	20.88 ± 1.39	52.62 ± 1.23	22.18 ± 1.05	52.74 ± 1.27	22.23 ± 1.06
AL-03	45°32′25″N 82°26′28″E	5	1.59 ± 0.03	4.5 ± 0.05	1.35 ± 0.01	5	2.05 ± 0.09	155.45 ± 9.57	76.01 ± 5.64	196.36 ± 7.61	96.02 ± 5.45	199.3 ± 7.09	97.46 ± 5.32
AL-04	45°21′38″N 82°38′21″E	1	1.69 ± 0.03	7.28 ± 0.05	1.89 ± 0.01	3	2.94 ± 0.12	5.65 ± 0.39	1.92 ± 0.16	7.7 ± 0.33	2.62 ± 0.16	7.87 ± 0.35	2.68 ± 0.16
AL-05	45°19′07″N 82°41′39″E	1.8	2.08 ± 0.04	9.45 ± 0.11	3.15 ± 0.01	5	4.26 ± 0.18	52.48 ± 4.6	12.31 ± 1.2	68.43 ± 3.43	16.05 ± 1.05	69.67 ± 3.43	16.34 ± 1.06

Note: OSL, optically stimulated luminescence; D is the environmental dose rate; De_{MAM} is the equivalent dose calculated by the minimum age model; De_{CAM} is the equivalent dose calculated by the median age model; De_{AVG} is the equivalent dose calculated by the average age model; Age_{MAM} is the optical luminescence age calculated by the minimum age model; Age_{CAM} is the optical luminescence age calculated by the median age model; and Age_{AVG} is the optical luminescence age calculated by the average age model.

4.3. The Southeast Section

The southeast section of the ALF extends for ~80 km from the northeast Lake Ebinur to study site 6 (Figure 2). Through remote sensing interpretation and field observations, it was revealed that there was a clear dextral strike-slip movement in this section. Study sites 1 to 7 were extensively investigated in order to describe their structures, as well as geomorphological characters, and to measure the vertical and horizontal displacements.

Site 1 is situated ~9 km northeast of Lake Ebinur, as shown in Figure 2. Fault strikes N30°W were found at site 1, with the main fault developing along the edge of the bedrock hill, while the branch cut through the alluvial fan (Figure 4a). There were four stages of alluvial fans (T1–T4) developed along the stream channel. T1 is the lowest geomorphic surface, only ~6 m above the stream bed, and developed on both sides of the fault. T2 is ~20 m above the stream bed, T3 is ~50 m above the stream bed, and T4 is ~60 m above the stream bed. T2 and T3 are only preserved on one side of the fault, but T4 is the highest and most widely geomorphic surface developed on both sides of the fault. The horizontal displacement of T4 was measured to be 10 ± 1 m along the main fault, and the obvious dextral offset of T4 was estimated to be 86 ± 4 m along the branch fault (Figure 4a,b); however, it was possible that the dextral displacement of 86 ± 4 m could have been exaggerated due to the collapse of the alluvial fan. Fault scarps clearly formed on T4, and the topographic profile A–A' was extracted to measure the vertical displacement, which indicated that the vertical displacement of T4 across the fault scarp is 5 ± 0.5 m (Figure 4c). On the southeast side of the stream channel, red Carboniferous granite thrust on yellow Neogene sandstone and gray Quaternary deposits (Figure 4d) are shown. The Neogene sandstone also shows larger vertical dislocations on the riser (Figure 4e).
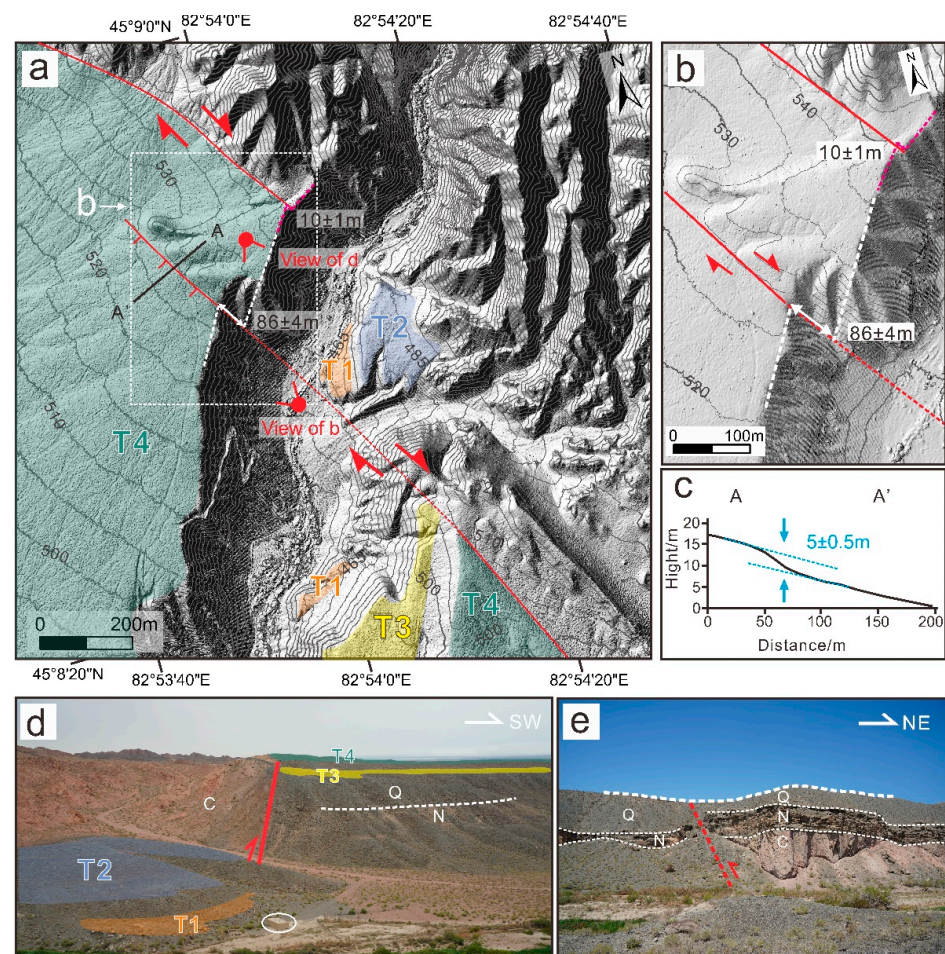

Figure 4. Site 1: (**a**) The hillshade map, which was built from a high-resolution UAV DEM using ArcGIS 10.8, shows structural and geomorphological characters of the Alakol Lake fault. The red

lines are the fault trace. The red dotted lines show that the fault traces are either unclear or covered. The red triangular arrows indicate dextral strike-slip movement. The black solid line (A–A') marks the location of the profile in (**c**). Four stages of alluvial fans (T1–T4) are developed along the stream channel, and the shadows with different colors depict the corresponding alluvial fans. The white dashed lines and the pink dashed lines represent the fit lines of the T4 riser. The white dotted box represents the range of (**b**). (**b**) The image of the hillshade map displays a detailed view of the geomorphic surface in (**a**). The white and pink dashed lines in the image represent the fit lines. The white and pink arrows indicate the preferred offset. (**c**) Topographic profile across the fault extracted from the UAV DEM was used to measure the vertical offset. The blue dashed lines are fit lines. (**d**) The field photo shows the fault trace and alluvial fans. The white oval highlights the house for scale. (**e**) The field photo was shot in the northwest. The red dashed line represents the fault. Q represents the alluvial fan deposits (probably middle–upper Pleistocene), N represents the Neogene sandstone, and C represents the Carboniferous granite.

Site 2 is located ~25 km northwest of site 1 (Figure 2). At this site, the fault trace strikes N45°W. A series of gullies and ridges were dextrally displaced in the N40°W direction by the ALF (Figure 5a). The horizontal displacement of two large gullies were measured to be 20 ± 4 m and 22 ± 1 m, respectively, while the horizontal displacement of the ridge was measured to be 30 ± 6 m. The vertical displacement of the fault scarp is 1.0 ± 0.1 m in the profile A–A' (Figure 5b). The black line B–B' shows another dextral ridge, and a road crosses the ridge along the location of the fault scarp (Figure 5a). The vertical displacement of the dextral ridge is 2.1 ± 0.2 m in the profile B–B' (Figure 5b).
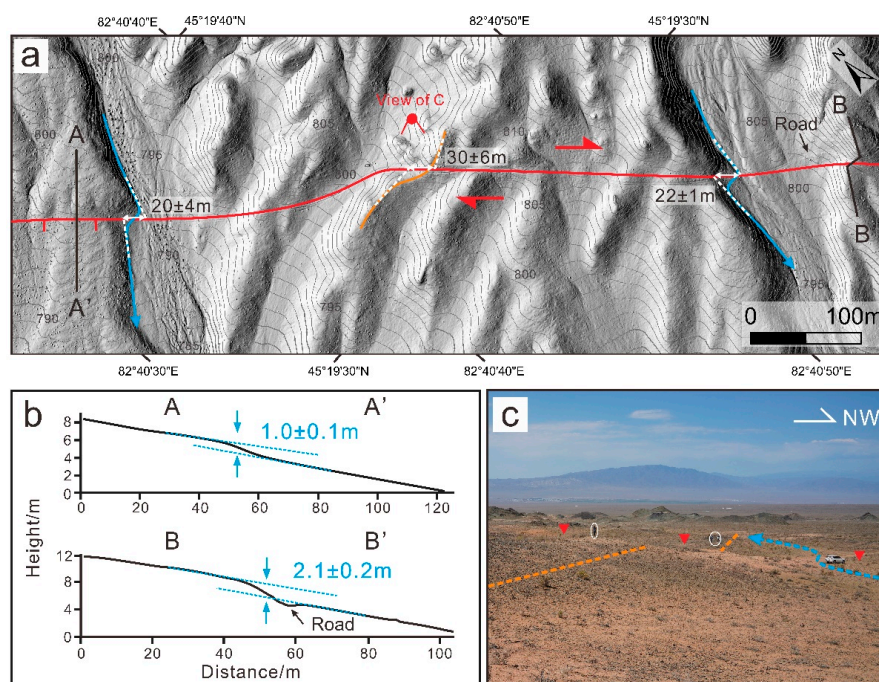

Figure 5. Site 2: (**a**) The hillshade map image, which was made using the high-resolution UAV DEM, shows the geomorphological expression of the Alakol Lake fault. The red lines are the fault trace. The red triangular arrows indicate dextral strike-slip movement. The two blue curves represent the horizontal offset of the gullies. The orange curve represents the dextrally displaced ridge. The black solid lines (A–A' and B–B') indicate the location of the extracted fault scarp. All of the white dashed lines represent the fit lines. The white arrows indicate the preferred offset. (**b**) Two topographic profiles across the fault extracted from the UAV DEM were used to measure the vertical offset. The blue dashed lines are fit lines. (**c**) The field photo shows the dextrally displaced ridge. The dotted orange lines show the location of the ridge. The red triangles indicate the fault trace. The blue dashed line indicates the dextral channel. The white ovals highlight the people for scale.

Site 3 is located ~1 km northwest of site 2 (Figure 2). Two stages of alluvial fans were interpreted at site 3. The fault was traced at T2 with an N40°W striking scarp and developed a micro-pull-apart basin at T1. The north edge of the T2 alluvial fan exhibits an apparent dextral offset of 34 ± 8 m at the erosional side, representing a minimum estimate of the displacement due to the possibility of the erosion of the channel (Figure 6a). Furthermore, a micro-pull-apart basin (~2 m deep, ~400 m long, and ~50 m wide) on T1 was controlled by a micro-stepover of the fault (Figure 6a,c). Two topographic profiles (A–A′ and B–B′) were extracted to measure the vertical displacement (Figure 6a,b). The topographic profile A–A′ of T1 indicates that the vertical displacement of the two fault scarps, in opposite directions, is 1.8 ± 0.1 m and 1.9 ± 0.4 m, respectively. The presence of two fault scarps in profile A–A′ primarily explains the existence of small pull-apart basins. Furthermore, the profile A–A′ across the pull-apart basin indicates almost no vertical displacement since T1 formed. The topographic profile B–B′ indicates that the vertical displacement across the fault scarps on T2 is 3.5 ± 0.9 m. Compared to the horizontal dislocations, the vertical displacement was not worth mentioning.
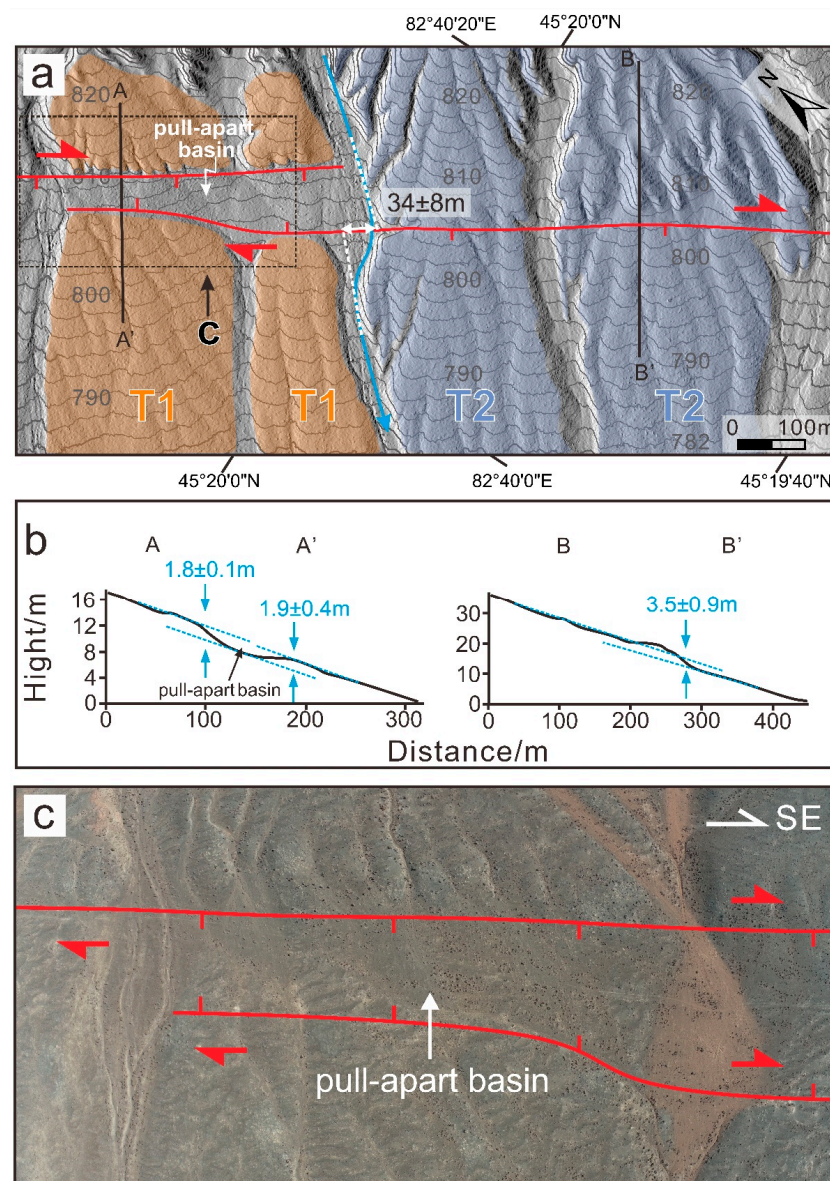

Figure 6. Site 3: (**a**) The hillshade map image, which was made using the high-resolution UAV DEM, shows the geomorphological expression of the Alakol Lake fault. The red lines are the fault trace,

and the scales indicate the slope direction of the fault scarp. The red triangular arrows indicate dextral strike-slip movement. The black dotted box represents the range of Figure c. The orange shadows represent T1, and purple shadows represent T2. The blue curves represent the dextrally displaced edge of the alluvial fans, and the white dashed lines represent the fit lines. The white arrows indicate the preferred offset. The black solid lines (A–A′ and B–B′) indicate the location of the extracted fault scarps. (**b**) Topographic profiles across the fault extracted from the UAV DEM were used to measure the vertical offset. The blue dashed lines are fit lines. (**c**) A photo taken by the drone shows the fault traces and a pull-apart basin.

Site 4 is located ~2 km northwest of site 3 (Figure 2). At site 4, two stages of alluvial fans were interpreted using the UAV DEM (Figure 7a). The horizontal displacement of two large subgullies was measured to be 20 ± 3 m and 18 ± 2 m, respectively, for the T2 alluvial fan (Figure 7a–c); however, 20 ± 3 m for the horizontal offset represented the minimum estimate of the displacement due to measurement on the erosion side of the channel. The topographic profiles (A–A′ and B–B′) indicate that the vertical displacements across the fault scarp are 0.7 ± 0.1 m and 2.6 ± 0.2 m, respectively (Figure 7d). The field photo shows the dextrally displaced gully and the fault scarp on the surface of the alluvial fan (Figure 7e). A clear fault scarp that has a distinct vertical displacement can be seen on the alluvial fan, as well as a series of subgullies (Figure 7f). In the field, a fault spring was found near the fault trace (Figure 7g). Many reeds and grasses grew around the spring and fixed a large amount of sand and soil.
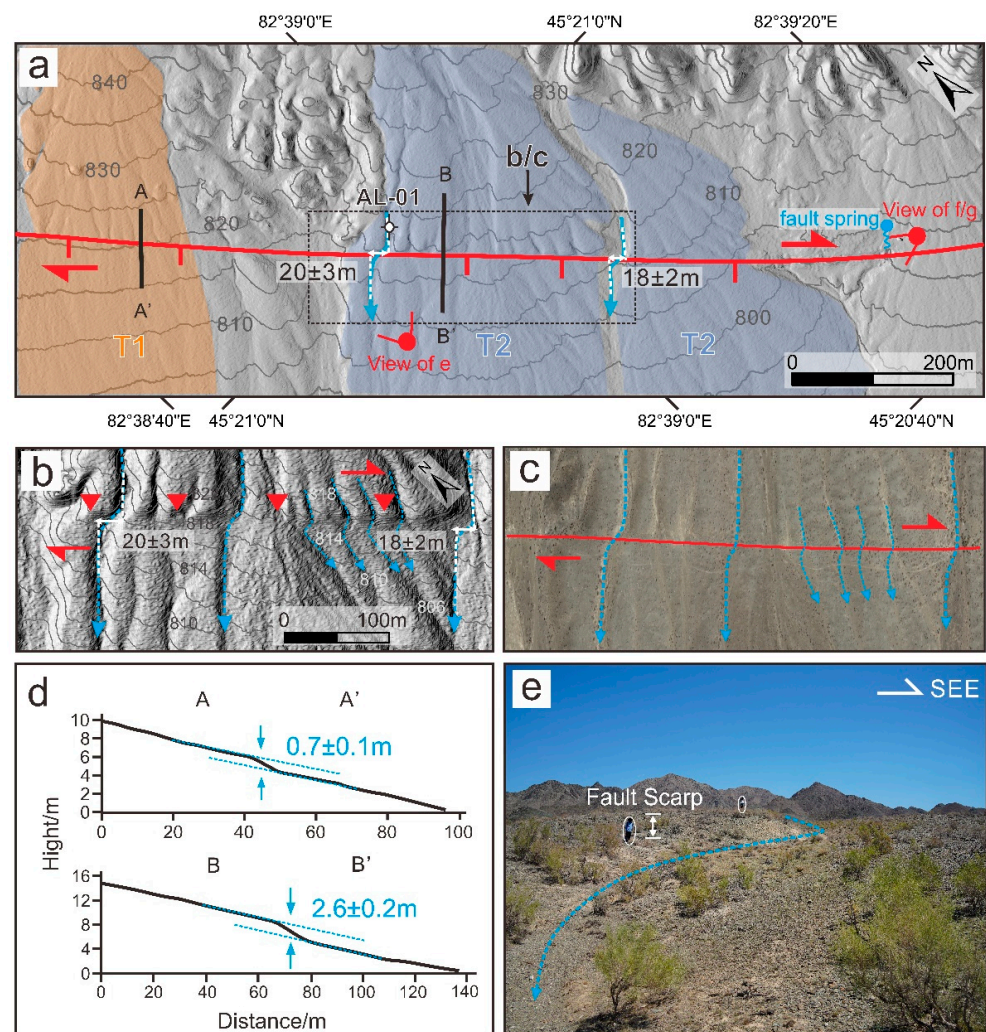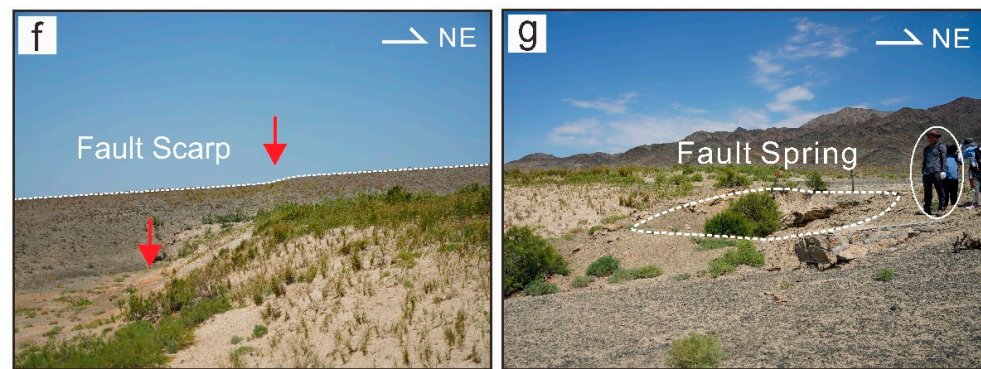

Figure 7. *Cont.*

Figure 7. Site 4: (**a**) The hillshade map image, which was made using the high-resolution UAV DEM, shows the geomorphological expression of the Alakol Lake fault. The red line is the fault trace, and the scales indicate the slope direction of the fault scarp. Two red triangular arrows indicate dextral strike-slip movement. The orange shadow represents T1, and the purple shadows represent T2. The blue curves with arrows represent the dextrally displaced gullies, and the white dashed lines represent the fit lines. The white arrows indicate the preferred offset. The spring symbol composed of the blue circle and blue curve indicates the location of the fault spring. The black solid lines (A–A′, B–B′) indicate the location of the extracted fault scarps. The black dotted box represents the range of (**b,c**). (**b**) The enlarged hillshade map image shows the more detailed geomorphic surface in (**a**). Four identical red triangles indicate the fault trace. (**c**) A field photo of the range corresponding to (**b**). (**d**) Topographic profiles across the fault extracted from the UAV DEM were used to measure the vertical offset. The blue dashed lines are fit lines. (**e**) The field photo shows the dextrally displaced gully and fault scarp. (**f**) The field photo shows the fault scarp. The dotted white line indicates the geomorphic surface. Two red arrows show the fault scarp. (**g**) The picture shows the fault spring in the field.

Site 5 is located ~26 km northwest of site 4 (Figure 2). Three stages of alluvial fans (T1–T3) developed along the stream channel at site 5 (Figure 8a,c). T1 is the lowest alluvial fan and is severely eroded, which is ~14 m above the stream bed; T2 is ~18 m above the stream bed; and T3 is the highest alluvial fan, which is ~24 m above the stream bed. The ALF separated into two strands, forming the fault scarp on T2. The obvious horizontal displacement of the T2 riser was measured to be 27 $\pm$ 6 m on the west strand fault, and an OSL sample AL-02 was collected to calculate the slip rate of the ALF. The topographic profile A–A′ indicates that T2 has already experienced two vertical dislocations due to the active fault, and the vertical displacement across the two different scarps is 1.6 $\pm$ 0.1 m and 3.8 $\pm$ 0.8 m (Figure 8b). The topographic profile B–B′ also indicates that the vertical displacement of T2 is 1.5 $\pm$ 0.4 m. The field photograph shows the field view of the alluvial fans and the fault scarps across T2 (Figure 8c).

Site 6 is situated ~10 km northwest of site 5 (Figure 2). The Pleiades DEM shows the fault trace along strikes N30°W (Figure 9a). At the north side of site 6, there is a stream channel that crosses the ALF. Along the river, there are three stages of alluvial fans, named T1, T2, and T4 (inferred from residual ridges of a similar height). (Figure 9b). T1 is the lowest alluvial fan and is ~6 m above the stream bed. T2 is ~18 m above the stream bed, while T4 is the highest alluvial fan, ~58 m above the stream channel. The obvious dextral offset of T4 was estimated to be 238 $\pm$ 30 m, representing the minimum estimate of the displacement due to the possibility of the erosion of the channel. Additionally, two gullies developed on T4, which were estimated in their horizontal displacement to be 212 $\pm$ 20 m and 195 $\pm$ 15 m, respectively. The photos show the exposed fault breccia, which indicates the Carboniferous bedrock fault at this site (Figure 9c,d). The bedrock fault dips to the NW and shows that the Carboniferous bedrock has thrust over the Quaternary strata.
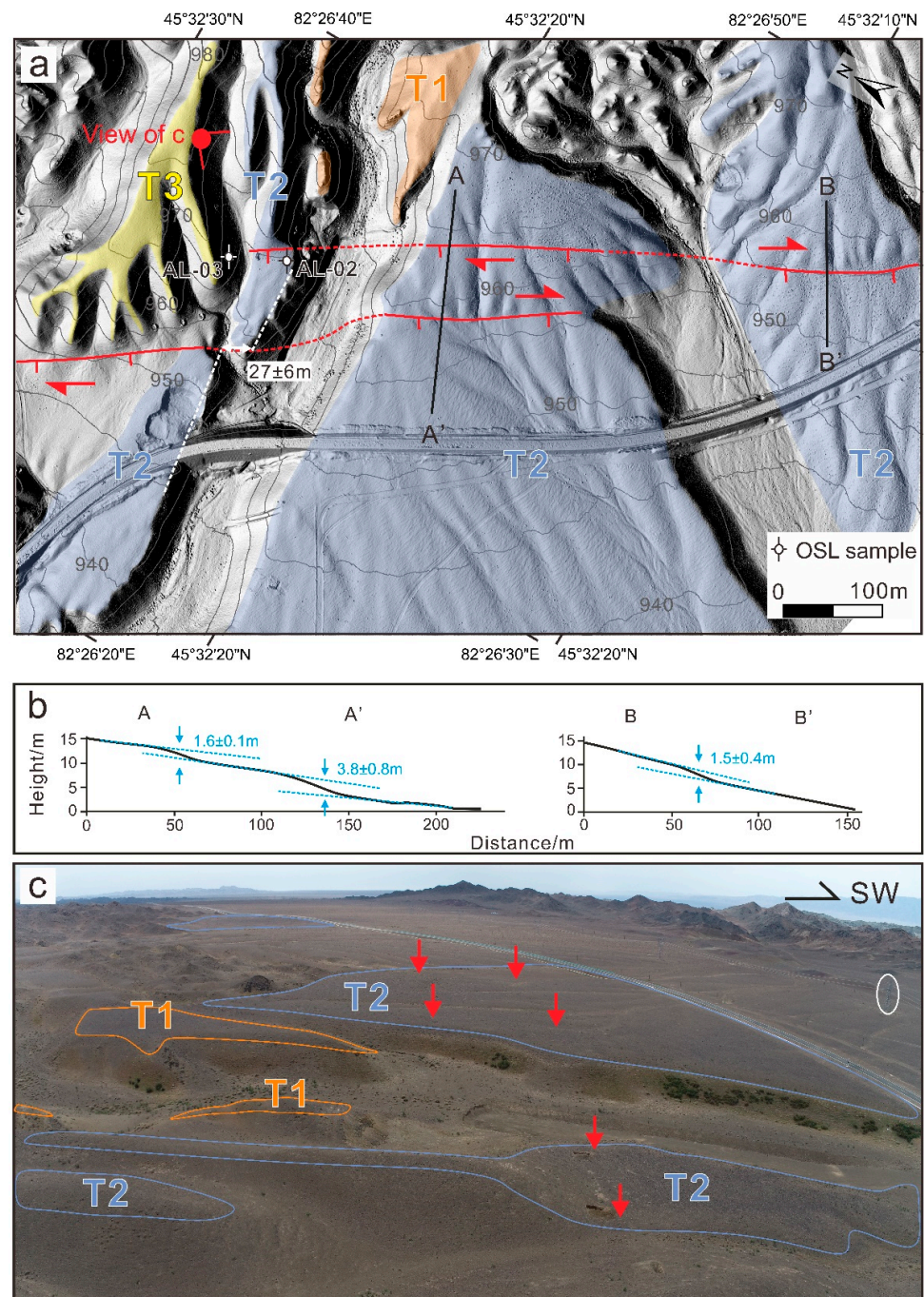
Figure 8. Site 5: (**a**) The hillshade map image, which was made using the high-resolution UAV DEM, shows the geomorphological expression of the Alakol Lake fault. Different colored shadows represent different alluvial fans. The red lines indicate clear fault traces, while the red dotted lines show fault traces that are either not visible or are covered. The white arrows indicate the preferred offset. The red triangular arrows indicate dextral strike-slip movement. The scales indicate the slope direction of the fault scarp. The white dashed lines represent the dextrally displaced T2 alluvial fan. The black solid lines (A–A′, B–B′) indicate the location of the extracted fault scarps. (**b**) Topographic profiles across the fault extracted from the UAV DEM were used to measure the vertical offset. The blue dashed lines are fit lines. (**c**) The field photo shows the fault trace and the different alluvial fans. The red arrows indicate the fault scarp and fault trace, and the white circle represents the iron tower as a reference.
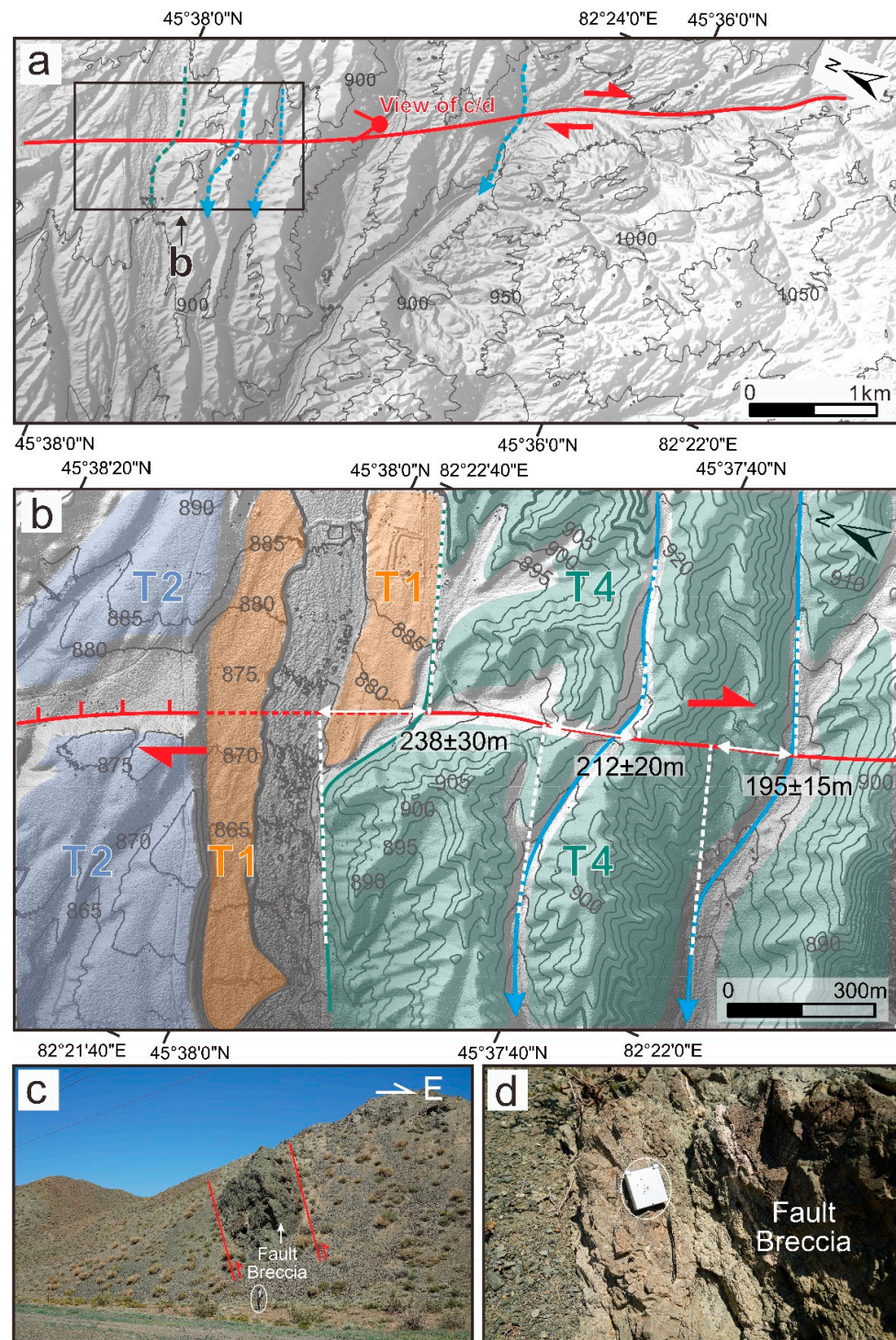
Figure 9. Site 6: (**a**) View of the Pleiades DEM shows the geomorphological expression of the Alakol Lake fault. (**b**) Hillshade map image, which was made using the high-resolution UAV DEM, shows the enlarged geomorphic surface. The red lines are the fault traces, and the red dotted lines show that the fault traces are not clear or are covered. The red triangular arrows indicate dextral strike-slip movement. The scales indicate the slope direction of the fault scarp. Different colored shadows represent different alluvial fans. The green curve represents the dextrally displaced alluvial fan. The blue curve represents the dextrally displaced gullies. All of the white dashed lines represent the fit lines. The white arrows indicate the preferred offset. (**c,d**) The fault breccia indicated by the white arrow revealed in the field.

Site 7 is between site 1 and site 2 (Figure 2), which shows four alluvial fans (at least equivalent to the T4 stage of the alluvial fan or older) at a large spatial scale from the view of the Pleiades DEM (Figure 10a). The fault strikes N42°W and develops along the edge of the bedrock hill. In the view, we mapped the range of the alluvial fans using the Pleiades satellite image and the DEM. The fan apex of the four alluvial fans was dextrally displaced relative to the stream channel. We roughly estimated the horizontal offset and uncertainty by measuring the distance from the stream bed to both sides of the alluvial fan edge. The horizontal offsets from fan 1 to fan 4 are 267 ± 60 m, 312 ± 131 m, 257 ± 73 m, and 233 ± 70 m, respectively (Figure 10).
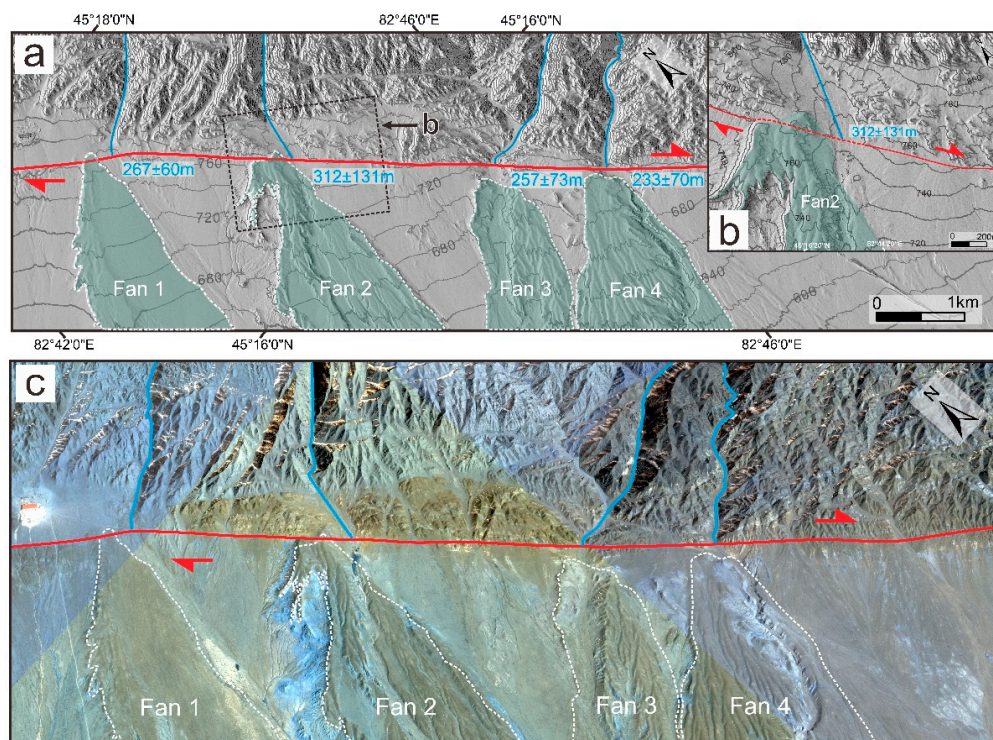

Figure 10. Site 7: (**a**) View of the Pleiades DEM shows some displaced alluvial fans. The translucent green shades are the alluvial fans. The red lines are the fault traces, and the red triangular arrows indicate dextral strike-slip movement. The blue curves represent the stream channels. (**b**) Hillshade map image, which was made by the high-resolution UAV DEM, shows the geomorphic surface of enlarged alluvial fan 2. (**c**) The outline of alluvial fans identified based on the texture and color characteristics in the Pleiades satellite image.

4.4. The Northwest Section

The northwest section is located on the eastern side of Lake Alakol and extends for ~70 km (Figure 2). To overcome the difficulty of obtaining information on the Kazakhstan section, Google Earth images and the Pleiades DEM are used to identify the fault trace and observe the horizontal displacement of the geomorphic surface.

Site 8 is located at the national boundary between China and Kazakhstan (Figure 2). The fault trace strikes N40°W, and some gullies that are dextrally displaced can be observed in the Pleiades DEM (Figure 11a,b). Because the alluvial fans are ~25 m above the channel, we estimated them to be T3 alluvial fans. The synchronous displacement of the three gullies and the offsets of T3 riser on the north side of the alluvial fans was estimated to be 56 ± 10 m according to the back-slipped method in the Pleiades DEM image (Figure 11c).
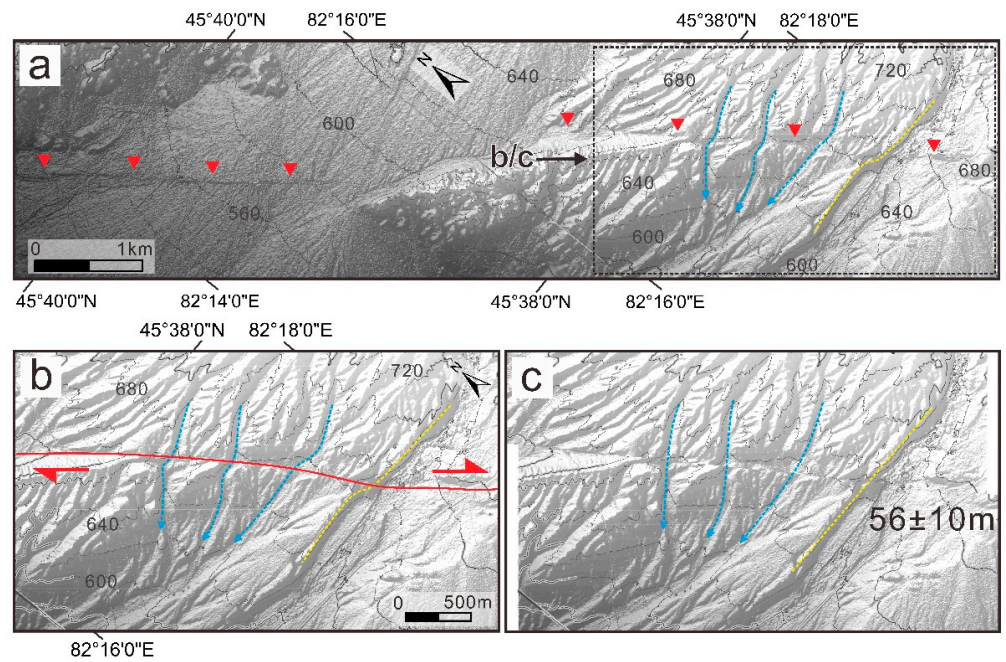
Figure 11. Site 8: (**a**) View of the Pleiades DEM shows the fault trace and the displaced geomorphic surface. The red triangles indicate the fault trace. The blue dashed lines indicate the displaced gullies, while the yellow dashed lines indicate the displaced T3 riser. (**b**) View of the enlarged geomorphic surface shows the displaced gullies. The red triangular arrows indicate dextral strike-slip movement. (**c**) The back-slipped view of the gullies.

Site 9 is located on the eastern shore of Lake Alakol (Figure 2). The northwest section of the ALF strikes N30°W and extends by ~25 km along the edge of Lake Alakol at this site (Figure 12a,b). Two topographic profiles (A–A′ and B–B′) across the fault extracted from the DEM indicate that the fault scarp is 5.6 ± 0.5 m and 2.6 ± 0.9 m, respectively (Figure 12a,c). A series of gullies were dextrally dislocated along the fault scarp, as interpreted from the Google Earth image. The horizontal displacement of these gullies was measured to be 76 ± 16 m, 68 ± 6 m, 51 ± 4 m, 27 ± 3 m, and 28 ± 1 m, respectively (Figure 12d,e); however, the lacustrine geomorphic surface near the lake shore does not correspond to the stages of the alluvial fans in our study.
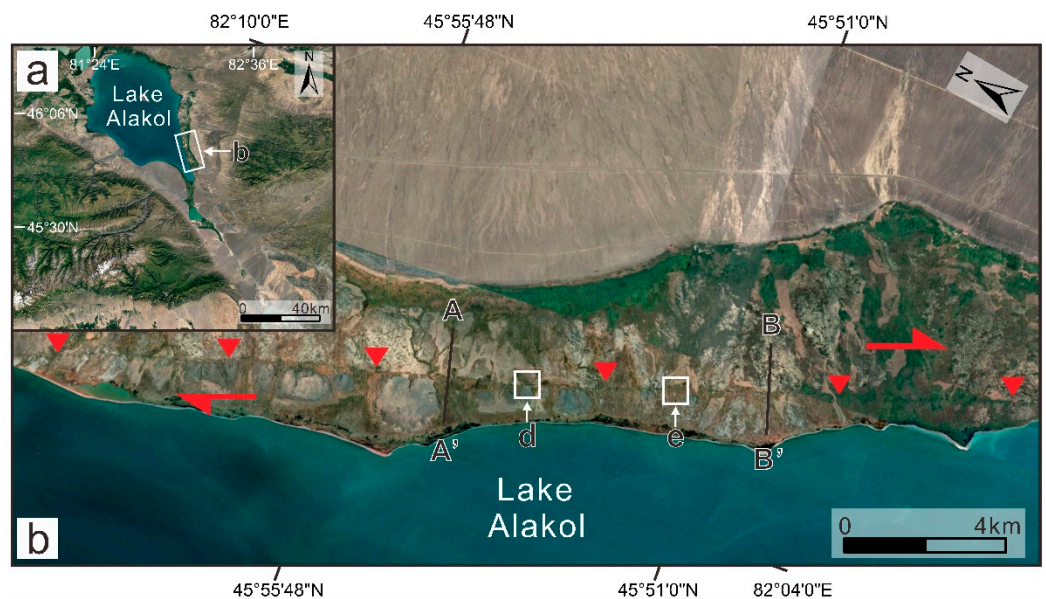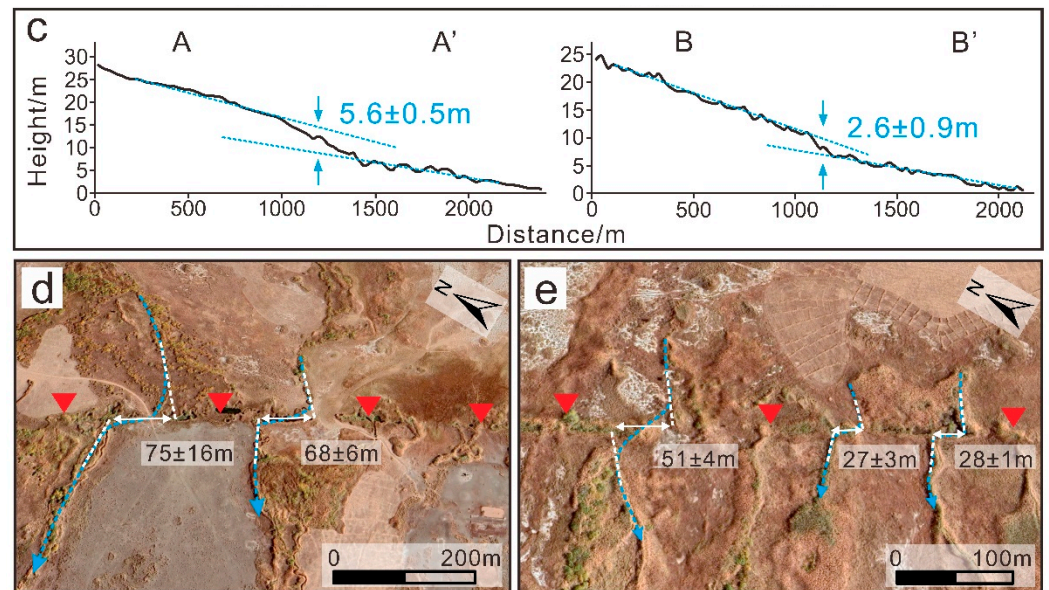

Figure 12. *Cont.*

Figure 12. Site 9: (**a**) The location of site 9 is shown on Google Earth. (**b**) The fault trace and geomorphic surface are shown on Google Earth. Six identical red triangles indicate the fault trace. Two red triangular arrows indicate dextral strike-slip movement. The black solid lines (A–A′ and B–B′) show where the topographic profiles were extracted. The white boxes represent the viewing areas of (**d**,**e**). (**c**) Topographic profiles (A–A′ and B–B′) across the fault extracted from the DEM were used to measure the vertical offset. The blue dashed lines are fit lines. (**d**,**e**) Some images of the displaced gullies taken on Google Earth. The blue dashed lines indicate the displaced gullies. The white dashed lines represent the fit lines. The white arrows indicate the preferred offset.

5. Discussion

5.1. Geometric Distribution and Movement Characteristics

The ALF is a NW-SE-trending dextral strike-slip fault. The ALF is situated along the northern margin of the Dzhungarian gate, stretching roughly 150 km from Lake Ebinur to Lake Alakol. Lake Alakol is located within the pull-apart basin of the stepover between the DZF and CF. According to the geometric distribution, the ALF seems to be a link fault crossing the stepover and connecting the southeast end of the CF to the DZF (Figure 13). The straight northeast lakeshore of Lake Alakol indicates that the ALF affects the topography of the pull-apart basin.

Numerous landforms, which include alluvial fans, stream channels, gullies, and ridges along the fault, have been found to be dextrally displaced. From the measured displacement of the geomorphic surfaces, the horizontal displacement is mostly tens of meters, and the horizontal displacement of certain alluvial fans even reaches almost a hundred meters. In contrast, the vertical displacement is mostly less than 5 m; therefore, the movement characteristic of the ALF is mainly a dextral strike-slip. At site 1 and site 6, the Carboniferous bedrock thrust over the Quaternary young strata with a high dip angle (Figures 4b,d and 7c). This indicates the southeast section of the ALF is characterized by shearing and compression.
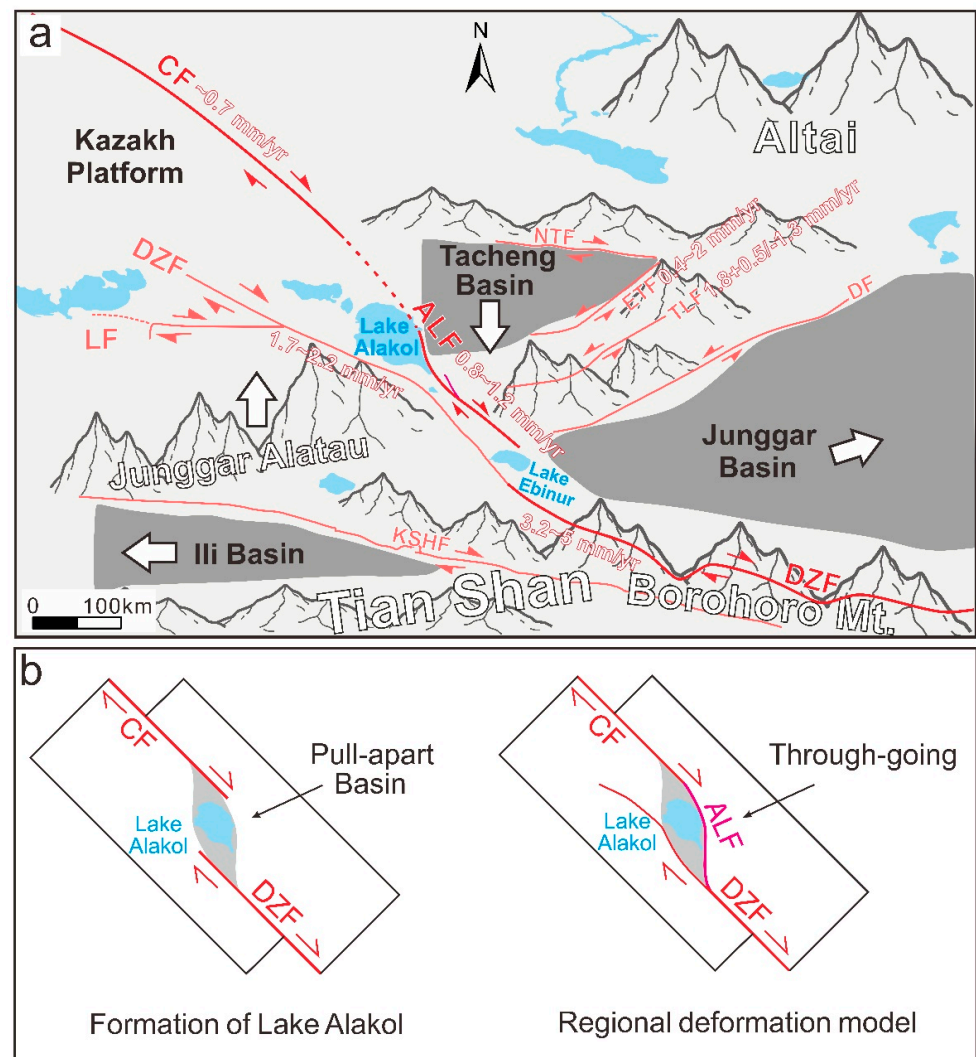
Figure 13. (**a**) Simplified geological model map of the new fault in the western Junggar. The white arrows indicate the relative movement directions of the Tacheng Basin, Junggar Alatau, and Junggar Basin. DZF—Dzhungarian fault; ALF—Alakol Lake fault; CF—Chingiz fault; LF—Lepsy fault; KSHF—Kashihe fault; DF—Daerbute fault; TLF—TuoLi fault; ETF—East Tacheng fault; and NTF—North Tacheng fault. (**b**) Evolutionary model map of Lake Alakol and the Alakol Lake fault.

5.2. Estimating the Slip Rate of the ALF

Many geomorphic surfaces were displaced dextrally along the ALF from site 1 to site 9. By measuring the displacement and dating these surfaces, the slip rate of the ALF can be estimated. At site 4, the dating age of the sample AL-01 represents the formation age of the T2 alluvial fan (Figures 3a and 7a,c), and the T2 riser displaced 20 ± 3 m of the horizontal offset (Figure 7a,c). We calculated a dextral strike-slip rate of 0.8 ± 0.2 mm/a. Considering the horizontal offset of 20 ± 3 m measured on the erosion side of the channel, the strike-slip rate of 0.8 ± 0.2 mm/a is lower than the actual value.

At site 5, the horizontal displacement of the T2 riser was measured to be 27 ± 6 m (Figure 8a), and an age for T2 of 22.23 ± 1.06 kyr was obtained by dating the sample AL-02 (Table 1); therefore, a dextral strike-slip rate of 1.2 ± 0.3 mm/a was calculated using the total horizontal offset and the T2 age.

Therefore, the Alakol Lake fault has a dextral strike-slip rate of 0.8–1.2 mm/a (closer to 1.2 mm/a). The strike-slip rate of the Alakol Lake fault is higher than that of the Chingiz fault in the northern region (~0.7 mm/a) (Figure 13) [33] but slower than that of the Dzhungarian fault in the southern region (3.2–5 mm/a) [19,20,30].

The slip rates of these dextral strike-slip faults indicate a gradual decrease from the Borohoro Mountain to the Kazakhstan platform. This result is consistent with the view that most of the shortening is absorbed within the Tian Shan based on the GPS data decreasing to the north and the view that the tectonic deformation of the Tian Shan decreases to the north [14,22–24].

5.3. Differential Movement of the Block at the North Side of the Tian Shan

The formation mechanism of the dextral strike-slip fault has great significance for the exploration of geodynamics. The GPS velocities display that the DZF and ALF accommodate ~2 mm/a of crustal shortening at the NE trending in the Dzhungarian gate (Figure 1c), and the horizontal-slip rates of the ALF (0.8–1.2 mm/a) and DZF (1.7–2.2 mm/a) at the NW trending are basically equivalent to the shortening of the NE trending. This indicates that the Junggar Alatau and the Tacheng Basin were oblique extruding. This movement characteristic is widespread on the north side of the Tian Shan and caused several NW-SE-trending dextral strike-slip faults to develop, including the Talas–Fergana fault (TFF) and the Dzhungarian fault, which have attracted much attention [2,19,20,27]. Campbell et al. (2013) and Hu et al. (2021) studied the slip rate of the Dzhungarian fault and concluded that the north–south crustal shortening in the Tian Shan is accommodated by the dextral strike-slip fault [19,20]. Rizza et al. (2019) studied the deformation mode of the Talas–Fergana fault based on the slip rate and concluded that the Talas–Fergana fault was subjected to the northward compression of the Pamir Plateau, resulting in counterclockwise rotation around the vertical axis of the fault [27]. We inferred that the ALF was also subjected to the northward compression and played an important role in accommodating the north–south crustal shortening. Affected by the Pamir Plateau wedging, the deformation of the Tian Shan decreases from west to east [2,3]; therefore, the Junggar Alatau moved northward with respect to the Tacheng Basin. By studying the East Tacheng fault (ETF), Yu et al. (2021) pointed out sinistral slip rates of 0.4–2.0 mm/a in the ETF, and Yuan et al. (2023) estimated sinistral slip rates of 1.8 + 0.5/-1.3mm/a in the TLF [17,71]. We can find that the slip rate of the ALF is close to these sinistral strike-slip faults. This implies that the Junggar Basin has moved northeastward with respect to the Tacheng Basin. Our study indicated that the Tacheng Basin moved southward and produced conjugate NE and NW strike-slip faults during the regional N-S shortening. The GPS velocities suggest that the Junggar Basin moves northeastward [17,28], which coordinates the southward movement of the Tacheng Basin and can also explain the formation of sinistral strike-slip faults in the western Junggar.

Based on preliminary estimates of the slip rate of the ALF, the ALF may replace the role of the northwest section of the DZF to transfer the crustal shortening to the further north Kazakhstan platform. Furthermore, on the south side of the northwest section of the DZF, the Lepsy fault also resolves part of the slip rate of the DZF [72]; therefore, the slip rate in the northwest section of the DZF shows a significant decrease compared with the east section. The northwest section of the DZF seems like a horsetail structure at the end of the strike-slip fault. Ultimately, we propose the model that the ALF serves as a connecting point for the Dzhungarian fault and the Chingiz fault, resulting in a mega NW-SE dextral strike-slip fault zone that extends more than 1400 km from the eastern side of the Borohoro Mountain to 500 km deep into the Kazakhstan platform (Figure 13).

6. Conclusions

The ALF extends at the northern margin of the Dzhungarian gate from Lake Alakol to Lake Ebinur for ~150 km. Numerous landforms, which include alluvial fans, stream channels, gullies, and ridges along the fault, are dextrally displaced, and the large horizontal/vertical offset ratio and straight fault traces indicated that the ALF is mainly a dextral strike-slip fault, which had significant activity in the late Quaternary. Based on the dislocation measurement and chronological dating of the geomorphic surface, the slip rates of the ALF are estimated at 0.8–1.2 mm/a (closer to 1.2 mm/a). The ALF serves as a connecting point for the Dzhungarian fault and the Chingiz fault, resulting in the formation

of a mega NW-SE dextral strike-slip fault zone. According to our analysis of the dating samples taken from the alluvial fan, as well as our measurement of the displacement of the alluvial fan and gullies, it appears that the Alakol Lake fault has a dextral sinistral slip rate of 0.8–1.2 mm/a (closer to 1.2 mm/a). The strike-slip rate of the Alakol Lake fault is comparatively higher than that of the Chingiz fault in the northern region (~0.7 mm/a) but slower than that of the Dzhungarian fault in the southern region (3.2–5 mm/a). The Chingiz–Alakol–Dzhungarian fault zone shows a gradual decrease in deformation towards the interior of the Kazakhstan platform.

References

1. Molnar, P.; Tapponnier, P. Cenozoic tectonics of Asia: Effects of a continental collision: Features of recent continental tectonics in Asia can be interpreted as results of the India-Eurasia collision. *Science* **1975**, *189*, 419–426. [CrossRef] [PubMed]
2. Tapponnier, P.; Molnar, P. Active faulting and Cenozoic tectonics of the Tien Shan, Mongolia, and Baykal regions. *J. Geophys. Res.* **1979**, *84*, 3245–3459. [CrossRef]
3. Avouac, J.P.; Tapponnier, P.; Bai, M.; You, H.; Wang, G. Active thrusting and folding along the northern Tien Shan and Late Cenozoic rotation of the Tarim relative to Dzungaria and Kazakhstan. *J. Geophys. Res. Solid Earth* **1993**, *98*, 6755–6804. [CrossRef]
4. Bande, A.; Sobel, E.R.; Mikolaichuk, A.; Torres Acosta, V. Talas–Fergana Fault Cenozoic timing of deformation and its relation to Pamir indentation. *Geol. Soc. Lond. Spec. Publ.* **2015**, *427*, 295–311. [CrossRef]
5. Bosboom, R.; Dupont-Nivet, G.; Huang, W.; Yang, W.; Guo, Z. Oligocene clockwise rotations along the eastern Pamir: Tectonic and paleogeographic implications. *Tectonics* **2014**, *33*, 53–66. [CrossRef]
6. Hendrix, M.S.; Dumitrn, T.A.; Graham, S.A. Late Oligocene-early Miocene unroofing in the Chinese Tian Shan: An early effect of the India-Asia collision. *Geology* **1994**, *22*, 487–490. [CrossRef]
7. Burchfiel, B.C.; Brown, E.T.; Deng, Q.; Feng, X.; Li, J.; Molnar, P.; Shi, J.; Wu, Z.; Yu, H. Crustal Shortening on the Margins of the Tien Shan, Xinjiang, China. *Int. Geol. Rev.* **1999**, *41*, 665–700. [CrossRef]
8. Deng, Q.; Feng, X.; Zhang, P.; Xu, X.; Peng, S.; Li, J. *Active Tectonics of Tianshan*; Seismological Press: Beijing, China, 2000. (In Chinese)
9. Li, C.; Wang, S.; Li, Y.; Chen, Y.; Sinclair, H.; Wei, D.; Ma, D.; Lu, H.; Wang, X.; Wang, L. Growth of the Tian Shan Drives Migration of the Conglomerate-Sandstone Transition in the Southern Junggar Foreland Basin. *Geophys. Res. Lett.* **2022**, *49*, e2021GL097545. [CrossRef]
10. Yang, X.; Li, Z.; Wang, W.; Zhang, P.; Wu, C.; Chen, G.; Duan, L.; Wu, X.; Liu, K. Quaternary Crustal Shortening of the Houyanshan Structure in the Eastern Chinese Tian Shan: Constrained from Geological and Geomorphological Analyses. *Remote Sens.* **2023**, *15*, 1603. [CrossRef]
11. Li, J.; Yao, Y.; Li, R.; Yusan, S.; Li, G.; Freymueller, J.T.; Wang, Q. Present-Day Strike-Slip Faulting and Thrusting of the Kepingtage Fold-and-Thrust Belt in Southern Tianshan: Constraints From GPS Observations. *Geophys. Res. Lett.* **2022**, *49*, e2022GL099105. [CrossRef]
12. Hu, Z.; Yang, X.; Li, A.; Yang, H.; Miao, S.; Yuan, H. Late Pleistocene slip rate and subsurface fault-plane geometry of the Latgan Fold (Bole Basin, North Tian Shan, NW China) derived from a deformed cosmogenically dated alluvial fan. *Geomorphology* **2023**, *421*, 108526. [CrossRef]
13. Yin, A.; Nie, S.; Craig, P.; Harrison, T.; Ryerson, F.; Xianglin, Q.; Geng, Y. Late Cenozoic tectonic evolution of the southern Chinese Tian Shan. *Tectonics* **1998**, *17*, 1–27. [CrossRef]
14. Thompson, S.C.; Weldon, R.J.; Rubin, C.M.; Abdrakhmatov, K.; Molnar, P.; Berger, G.W. Late Quaternary slip rates across the central Tien Shan, Kyrgyzstan, central Asia. *J. Geophys. Res. Solid Earth* **2002**, *107*, ETG 7-1–ETG 7-32. [CrossRef]

15. Peng, Z.; Graveleau, F.; Vendeville, B.C.; Wang, X.; Averbuch, O. Interaction between basement inherited strike-slip structures and thrust wedge propagation in the northern Tianshan foreland basin: Insight from analogue modelling experiments. *J. Struct. Geol.* **2024**, *183*, 105143. [CrossRef]

16. Selander, J.; Oskin, M.; Ormukov, C.; Abdrakhmatov, K. Inherited strike-slip faults as an origin for basement-cored uplifts: Example of the Kungey and Zailiskey ranges, northern Tian Shan. *Tectonics* **2012**, *31*, 4. [CrossRef]

17. Yu, J.; Walker, R.T.; Rhodes, E.J.; Zhang, P.; Li, C.; Wang, S.; Wang, Y.; Liu, F.; Hao, Y. East Tacheng (Qoqek) Fault Zone: Late Quaternary Tectonics and Slip Rate of a Left-Lateral Strike-Slip Fault Zone North of the Tian Shan. *Tectonics* **2021**, *40*, e2020TC006377. [CrossRef]

18. Burtman, V.S.; Skobelev, S.F.; Molnar, P. Late Cenozoic slip on the Talas-Ferghana fault, the Tien Shan, central Asia. *Geol. Soc. Am. Bull.* **1996**, *108*, 1004–1021. [CrossRef]

19. Campbell, G.; Walker, R.; Abdrakhmatov, K.; Schwenninger, J.; Jackson, J.; Elliott, J.; Copley, A. The Dzhungarian fault: Late Quaternary tectonics and slip rate of a major right-lateral strike-slip fault in the northern Tien Shan region. *J. Geophys. Res. Solid Earth* **2013**, *118*, 5681–5698. [CrossRef]

20. Hu, Z.; Yang, X.; Yang, H.; Huang, W.; Wu, G.; Miao, S.; Zhang, L. Slip rate and paleoseismology of the Bolokenu-Aqikekuduk (Dzhungarian) right-lateral strike-slip fault in the northern Tian Shan, NW China. *Tectonics* **2021**, *40*, e2020TC006604. [CrossRef]

21. Abdrakhmatov, K.Y.; Aldazhanov, S.A.; Hager, B.H.; Hamburger, M.W.; Herring, T.A.; Kalabaev, K.B. Relatively recent construction of the Tien Shan inferred from GPS measurements of present-day crustal deformation rates. *Nature* **1996**, *384*, 450–453. [CrossRef]

22. Zubovich, A.V.; Wang, X.; Scherba, Y.G.; Schelochkov, G.G.; Reilinger, R.; Reigber, C.; Mosienko, O.I.; Molnar, P.; Michajljow, W.; Makarov, V.I.; et al. GPS velocity field for the Tien Shan and surrounding regions. *Tectonics* **2010**, *29*, e2010tc002772. [CrossRef]

23. Wang, M.; Shen, Z.K. Present-Day Crustal Deformation of Continental China Derived From GPS and Its Tectonic Implications. *J. Geophys. Res. Solid Earth* **2020**, *125*, e2019JB018774. [CrossRef]

24. Wu, C.; Zhang, P.; Zhang, Z.; Zheng, W.; Xu, B.; Wang, W.; Yu, Z.; Dai, X.; Zhang, B.; Zhang, K. Slip partitioning and crustal deformation patterns in the Tianshan orogenic belt derived from GPS measurements and their tectonic implications. *Earth-Sci. Rev.* **2023**, *238*, 104362. [CrossRef]

25. Tsai, C.H.; Abdrakhmatov, K.; Mukambayev, A.; Elliott, A.J.; Elliott, J.R.; Grützner, C.; Rhodes, E.J.; Ivester, A.H.; Walker, R.T.; Wilkinson, R. Probing the Upper End of Intracontinental Earthquake Magnitude: A Prehistoric Example From the Dzhungarian and Lepsy Faults of Kazakhstan. *Tectonics* **2022**, *41*, e2022TC007300. [CrossRef]

26. Li, A.; Ran, Y.; Gomez, F.; Thompson Jobe, J.A.; Liu, H.; Xu, L. Segmentation of the Kepingtage thrust fault based on paleoearthquake ruptures, southwestern Tianshan, China. *Nat. Hazards* **2020**, *103*, 1385–1406. [CrossRef]

27. Rizza, M.; Abdrakhmatov, K.; Walker, R.; Braucher, R.; Guillou, V.; Carr, A.S.; Campbell, G.; McKenzie, D.; Jackson, J.; Aumaître, G.; et al. Rate of Slip From Multiple Quaternary Dating Methods and Paleoseismic Investigations Along the Talas-Fergana Fault: Tectonic Implications for the Tien Shan Range. *Tectonics* **2019**, *38*, 2477–2505. [CrossRef]

28. Wu, C.; Wang, W.; Zheng, W.; Zhang, P.; Yu, Z. Opposite Sense of Strike-Slip Faulting and Crustal Rotation Accommodating Left-Lateral Shear Between the Tianshan Mountains and Kazakh Platform. *Geophys. Res. Lett.* **2021**, *48*, e2021GL096442. [CrossRef]

29. Shen, J.; Wang, Y.; Li, Y. Characteristics of the Late Quaternary right-lateral strike-slip movement of Bolokenu-Aqikekuduk fault in northern Tianshan Mountains, NW China. *Geosci. Front.* **2011**, *2*, 519–527. [CrossRef]

30. Tsai, C.H.; Walker, R.; Daout, S.; Abdrakhmatov, K.; Mukambayev, A.; Grützner, C.; Rhodes, E. Palaeo-earthquake magnitudes on the Dzhungarian fault, N. Tien shan, and implications for the rupture processes of intraplate strike-slip faults. In Proceedings of the EGU2020: Sharing Geoscience, Online, 4–8 May 2020. [CrossRef]

31. Samygin, S.G. *Chingiz Wrench Fault and Its Role in the Structure of Central Kazakhstan*; Nauka Publishing House: Moscow, Russia, 1974. (In Russian)

32. Mukambayev, A.S.; Mikhailova, N.N. Seismic hazard of the main Chingiz fault for the territory of Semipalatinsk test site. *NNC RK Bull.* **2015**, *3*, 82–86, (In Russian with English Abstract).

33. Li, Y.; Liu, M.; Hao, M.; Zhu, L.; Cui, D.; Wang, Q. Active crustal deformation in the Tian Shan region, central Asia. *Tectonophysics* **2021**, *811*, 228868. [CrossRef]

34. Xu, X.; Han, Z.; Yang, X.; Zhang, S.; Yu, G.; Zhou, B.; Li, F.; Ma, B.; Chen, G.; Ran, Y. *Seimotectonic Map of China and Its Adjacent Regions*; Seismological Publishing Press: Beijing, China, 2016. (In Chinese)

35. Xiao, W.; Han, C.; Yuan, C.; Sun, M.; Lin, S.; Chen, H.; Li, Z.; Li, J.; Sun, S. Middle Cambrian to Permian subduction-related accretionary orogenesis of Northern Xinjiang, NW China: Implications for the tectonic evolution of central Asia. *J. Asian Earth Sci.* **2008**, *32*, 102–117. [CrossRef]

36. Xiao, W.; Santosh, M. The western Central Asian Orogenic Belt: A window to accretionary orogenesis and continental growth. *Gondwana Res.* **2014**, *25*, 1429–1444. [CrossRef]

37. Wang, Y.; Wang, Y.; Yin, J.; Thomson, S.N.; Xiao, W.; He, Z.; Chen, W.; Cai, K.; Wu, M.; Meng, Y. Mesozoic exhumation of the northern West Junggar, NW China: Insights from low-temperature thermochronometers. *Tectonophysics* **2023**, *862*, 229939. [CrossRef]

38. Buckman, S.; Aitchison, J.C. Tectonic evolution of Palaeozoic terranes in west Junggar, Xinjiang, NW China. *Geol. Soc. Lond. Spec. Publ.* **2004**, *226*, 101–129. [CrossRef]

39. Choulet, F.; Faure, M.; Cluzel, D.; Chen, Y.; Lin, W.; Wang, B. From oblique accretion to transpression in the evolution of the Altaid collage: New insights from West Junggar, northwestern China. *Gondwana Res.* **2012**, *21*, 530–547. [CrossRef]

40. Wu, C.; Hong, T.; Xu, X.; Wang, C.; Dong, L. A-type granites induced by a breaking-off and delamination of the subducted Junggar oceanic plate, West Junggar, Northwest China. *China Geol.* **2022**, *4*, 457–474. [CrossRef]

41. Chen, B.; Jahn, B. Genesis of post-collisional granitoids and basement nature of the Junggar Terrane, NW China: Nd-Sr isotope and trace element evidence. *J. Asian Earth Sci.* **2004**, *23*, 691–703. [CrossRef]

42. Zhu, Y.; Chen, B.; Xu, X.; Qiu, T.; An, F. A new geological map of the West Junggar, north Xinjiang (NW China): Implications for Paleoenvironmental reconstruction. *Episodes* **2013**, *36*, 205–220. [CrossRef] [PubMed]

43. Zheng, B.; Han, B.F.; Wang, Z.Z.; Liu, B.; Feng, L.X. An example of Phanerozoic continental crustal growth: The West Junggar Orogenic Belt, Northwest China. *Lithos* **2020**, *376–377*, 105745. [CrossRef]

44. Hu, A.; Wang, Z.; Xu, G. *Geologic Evolution, Petrogenesis and Metallgenesis in Northern XinJiang*; Science Press: Beijing, China, 1997; pp. 9–104. (In Chinese)

45. Chen, Y.; Hu, A.; Zhang, G.; Zhang, Q. Zircon U-Pb age and Sr-Nd isotopic composition of granitic genesis and its geological implications from Percambrian window of western Tianshan, NW China. *Geochimica* **1999**, *28*, 515–519. (In Chinese with English Abstract)

46. Chen, J.; Zhou, T.; Xie, Z.; Zhang, X.; Guo, X. Formation of positive εNd(T) granitoids from the Alataw Mountains, Xinjiang, China, by mixing and fractional crystallization: Implication for Phanerozoic crustal growth. *Tectonophysics* **2000**, *328*, 53–67. [CrossRef]

47. Yin, J.; Wang, Y.; Hodges, K.V.; Xiao, W.; Thomson, S.N.; Chen, W.; Yuan, C.; Sun, M.; Cai, K.; Sun, J. Episodic Long-Term Exhumation of the Tianshan Orogenic Belt: New Insights From Multiple Low-Temperature Thermochronometers. *Tectonics* **2023**, *42*, e2022TC007469. [CrossRef]

48. Arrowsmith, J.R.; Zielke, O. Tectonic geomorphology of the San Andreas Fault zone from high resolution topography: An example from the Cholame segment. *Geomorphology* **2009**, *113*, 70–81. [CrossRef]

49. Zielke, O.; Arrowsmith, J.R.; Grant Ludwig, L.; Akciz, S.O. High-Resolution Topography-Derived Offsets along the 1857 Fort Tejon Earthquake Rupture Trace, San Andreas Fault. *Bull. Seismol. Soc. Am.* **2012**, *102*, 1135–1154. [CrossRef]

50. Bahrami, S.; Stokes, M. Analyzing drainage basin orientation and its relationship to active fold growth (Handun anticline, Zagros, Iran). *Geomorphology* **2023**, *426*, 108605. [CrossRef]

51. Bi, H.; Zheng, W.; Ren, Z.; Zeng, J.; Yu, J. Using an unmanned aerial vehicle for topography mapping of the fault zone based on structure from motion photogrammetry. *Int. J. Remote Sens.* **2017**, *38*, 2495–2510. [CrossRef]

52. James, M.R.; Robson, S. Straightforward reconstruction of 3D surfaces and topography with a camera: Accuracy and geoscience application. *J. Geophys. Res. Earth Surf.* **2012**, *117*, e2011jf002289. [CrossRef]

53. Johnson, K.; Nissen, E.; Saripalli, S.; Arrowsmith, J.R.; McGarey, P.; Scharer, K.; Williams, P.; Blisniuk, K. Rapid mapping of ultrafine fault zone topography with structure from motion. *Geosphere* **2014**, *10*, 969–986. [CrossRef]

54. Kovanič, Ľ.; Štroner, M.; Blistan, P.; Urban, R.; Boczek, R. Combined ground-based and UAS SfM-MVS approach for determination of geometric parameters of the large-scale industrial facility—Case study. *Measurement* **2023**, *216*, 112994. [CrossRef]

55. Bemis, S.P.; Micklethwaite, S.; Turner, D.; James, M.R.; Akciz, S.; Thiele, S.T.; Bangash, H.A. Ground-based and UAV-Based photogrammetry: A multi-scale, high-resolution mapping tool for structural geology and paleoseismology. *J. Struct. Geol.* **2014**, *69*, 163–178. [CrossRef]

56. Wang, S.; Ren, Z.; Wu, C.; Lei, Q.; Gong, W.; Ou, Q.; Zhang, H.; Ren, G.; Li, C. DEM generation from Worldview-2 stereo imagery and vertical accuracy assessment for its application in active tectonics. *Geomorphology* **2019**, *336*, 107–118. [CrossRef]

57. Zhou, Y.; Parsons, B.; Elliott, J.R.; Barisin, I.; Walker, R.T. Assessing the ability of Pleiades stereo imagery to determine height changes in earthquakes: A case study for the E Mayor-Cucapah epicentral area. *J. Geophys. Res. Solid Earth* **2015**, *120*, 8793–8808. [CrossRef]

58. McCalpin, J. *Paleoseismology*, 2nd ed.; Academic Press: San Diego, CA, USA, 1996.

59. Zielke, O.; Klinger, Y.; Arrowsmith, J.R. Fault slip and earthquake recurrence along strike-slip faults—Contributions of high-resolution geomorphic data. *Tectonophysics* **2015**, *638*, 43–62. [CrossRef]

60. Scharer, K.M.; Salisbury, J.B.; Arrowsmith, J.R.; Rockwell, T.K. Southern San Andreas Fault Evaluation Field Activity: Approaches to Measuring Small Geomorphic Offsets—Challenges and Recommendations for Active Fault Studies. *Seismol. Res. Lett.* **2014**, *85*, 68–76. [CrossRef]

61. Bi, H.; Zheng, W.; Lei, Q.; Zeng, J.; Zhang, P.; Chen, G. Surface Slip Distribution Along the West Helanshan Fault, Northern China, and Its Implications for Fault Behavior. *J. Geophys. Res. Solid Earth* **2020**, *125*, e2020jb019983. [CrossRef]

62. Sieh, K.E. Slip along the San Andreas fault associated with the great 1857 earthquake. *Bull. Seismol. Soc. Am.* **1978**, *68*, 1421–1448.

63. Zielke, O.; Arrowsmith, J.R.; Ludwig, L.G. Slip in the 1857 and earlier large earthquakes along the Carrizo Plain, San Andreas Fault. *Science* **2010**, *327*, 1119–1122. [CrossRef] [PubMed]

64. Wang, X.; Lu, Y.; Zhao, H. On the performances of the single-aliquot regenerative-dose (SAR) protocol for Chinese loess: Fine quartz and polymineral grains. *Radiat. Meas.* **2006**, *41*, 1–8. [CrossRef]

65. Murray, A.S.; Wintle, A.G. Luminescence dating of quartz using an improved single-aliquot regenerative-dose protocol. *Radiat. Meas.* **2000**, *32*, 57–73. [CrossRef]

66. Wintle, A.G.; Murray, A.S. A review of quartz optically stimulated luminescence characteristics and their relevance in single-aliquot regeneration dating protocols. *Radiat. Meas.* **2006**, *41*, 369–391. [CrossRef]

67. Aitken, M.J. *An Introduction to Optical Dating*; Oxford University Press: Oxford, Britain, 1998.

68. Lu, Y.; Wang, X.; Wintle, A.G. A new OSL chronology for dust accumulation in the last 130,000 yr for the Chinese Loess Plateau. *Quat. Res.* **2007**, *67*, 152–160. [CrossRef]

69. Murray, A.S.; Wintle, A.G. The single aliquot regenerative dose protocol: Potential for improvements in reliability. *Radiat. Meas.* **2003**, *37*, 377–381. [CrossRef]

70. Prescott, J.R.; Hutton, J.T. Cosmic ray contributions to dose rates for luminescence and ESR dating: Large depths and long-term time variations. *Radiat. Meas.* **1994**, *23*, 497–500. [CrossRef]

71. Yuan, H.; Li, A.; Huang, W.; Hu, Z.; Zuo, Y.; Yang, X. Geological deformation of the TuoLi fault in the west Junggar since the late Quaternary. *Seismol. Geol.* **2023**, *45*, 49–66, (In Chinese with English Abstract).

72. Campbell, G.E.; Walker, R.T.; Abdrakhmatov, K.; Jackson, J.; Elliott, J.R.; Mackenzie, D.; Middleton, T.; Schwenninger, J.L. Great earthquakes in low strain rate continental interiors: An example from SE Kazakhstan. *J. Geophys. Res. Solid Earth* **2015**, *120*, 5507–5534. [CrossRef]